

STABILITY ESTIMATES FOR LINEARIZED NEAR-FIELD PHASE RETRIEVAL IN X-RAY PHASE CONTRAST IMAGING*

SIMON MARETZKE[†] AND THORSTEN HOHAGE[‡]

Abstract. Propagation-based X-ray phase contrast enables nanoscale imaging of biological tissue by probing not only the attenuation, but also the real part of the refractive index of the sample. Since only intensities of diffracted waves can be measured, the main mathematical challenge consists in a phase-retrieval problem in the near-field regime. We treat an often used linearized version of this problem known as contract transfer function model. Surprisingly, this inverse problem turns out to be well-posed assuming only a compact support of the imaged object. Moreover, we establish bounds on the Lipschitz stability constant. In general this constant grows exponentially with the Fresnel number of the imaging setup. However, both for homogeneous objects, characterized by a fixed ratio of the induced refractive phase shifts and attenuation, and in the case of measurements at two distances, a much more favorable algebraic dependence on the Fresnel number can be shown. In some cases we establish order optimality of our estimates.

Key words. stability, inverse problem, phase retrieval, X-ray phase contrast, contrast transfer function, support constraint

AMS subject classifications. 78A45, 78A46

1. Introduction. Over the past two decades, the dramatic increase in coherence and brightness of large-scale X-ray sources, such as third generation synchrotrons and free-electron-lasers, has paved the way for X-ray phase contrast imaging [31]. Classical X-ray radiography is limited to measuring the attenuation experienced by radiation traversing the probed object. Writing the refractive index in the X-ray physics notation $n = 1 - \delta + i\beta$ with $0 \leq \beta, \delta \ll 1$, this amounts to imaging β . Phase contrast techniques additionally probe the real-valued decrement δ of n , which induces phase shifts in the transmitted X-ray wave field. This enables imaging of biological cells and other micro-scale light-element specimen, for which $\beta \ll \delta$ holds in the hard X-ray regime [7, 27, 34, 44]. Owing to the small wavelength of X-rays, nano-scale spatial resolutions can be achieved as has been demonstrated down to 20 nanometers [2]. Moreover, phase contrast imaging can be combined with tomography, capable of resolving the refractive index of an unknown object in 3D [3, 17, 19, 20, 26, 38].

Unfortunately, the refractive phase shifts of the X-ray field cannot be observed directly by common CCD detectors due to their physical limitation to measuring wave intensities, i.e. the squared modulus of the wave field. In propagation-based phase contrast imaging, also known as *inline holography*, the required phase-sensitivity is achieved simply by free-space propagation without any optical elements: if the detector is placed in some finite distance down-stream of the sample, the imprinted phase shifts in the object's exit plane ($z = 0$ in Figure 1(b)) are partially encoded into measurable intensities by *diffraction*, i.e. self-interference of the wave field. We assume that the diffraction pattern or *hologram* is recorded in the optical near-field of the sample so that propagation is described by the Fresnel propagator [32]. In particular, we do not consider the corresponding far-field setup (coherent diffractive

*Published as: SIAM J. Appl. Math. (2017), 77(2), 384–408. DOI:10.1137/16M1086170

Funding: This work was funded Deutsche Forschungsgemeinschaft DFG through Project C02 of SFB 755 - Nanoscale Photonic Imaging

[†]Institute for Numerical and Applied Mathematics, University of Göttingen, Lotzestr. 16-18, 37083 Göttingen, Germany (s.maretzke@math.uni-goettingen.de).

[‡]Institute for Numerical and Applied Mathematics, University of Göttingen, Lotzestr. 16-18, 37083 Göttingen, Germany (hohage@math.uni-goettingen.de).

imaging, see e.g. [28,36]), where the data is given by Fourier magnitudes.

In this work, we are thus concerned with the reconstruction of the (generally complex-valued) wave-field perturbation h induced by the object from measured near-field intensities I . As this implicitly amounts to recovering the lost phase information in the data, i.e. to solving a *phase retrieval* problem, the question immediately arises whether the image recovery is actually *unique* and *stable*. Indeed, it is commonly argued [5,17,30] that diffraction patterns from at least two different sample-detector distances are required for a unique reconstruction of the imprinted phase shifts and attenuation. Assuming a *support constraint*, however, i.e. under the often physically reasonable assumption that the image h is non-zero only in compact subdomain of the field of view, we could show uniqueness of the reconstruction from a *single* hologram in [25] - even if h is complex-valued (see also [18] for a uniqueness result for the Helmholtz equation with real-valued n from phaseless near-field data in an interval of frequencies). In [26], such a reconstruction of a compactly supported complex image is demonstrated for simulated and experimental data, which turns out to be feasible, yet susceptible to low-frequency artifacts. Support constraints have also been found to stabilize image reconstruction in simpler settings where the probed object can be assumed to be completely non-absorbing [3,11].

These observations call for a better understanding of the *stability* of the considered near-field phase retrieval problem, which is the goal of this paper. We do so within a linearization of the relation between image h and the resulting intensity data I , valid for sufficiently “small” h , i.e. for weakly interacting objects similarly as in a recent stability analysis of domain reconstructions in phaseless inverse scattering [1]. The linearization is known as *contrast transfer function* model [12,42] and frequently applied in X-ray phase contrast imaging [7,13,15,20,21]. In this work, we analyze the arising linear forward operator T under the assumption that h has compact support. We prove that the associated inverse problem is not only unique but even *well-posed* in the sense that the recovered image h depends continuously on the measured data Th , i.e. finite data errors lead to bounded deviations in the recovered h . This result, which is quite surprising for an inverse problem with remote measurements, is achieved by relating the setting to a reconstruction from incomplete Fourier data. By the same technique we also derive explicit *stability estimates*, bounding the reconstruction error that results from a given data noise level in terms of the dimensionless Fresnel number.

In general, we find that the stability constant decays exponentially with the Fresnel number f and thus hardly gives any useful stability bounds for many experimental X-ray phase contrast setups. However, we establish much more favorable $\mathcal{O}(f^{-1})$ - and even $\mathcal{O}(f^{-1/2})$ -decay rates in two relevant situations: The first assumes proportionality of the real and the imaginary part of the image h , which occurs e.g. for single-material and non-absorbing samples. The second situation concerns general objects, but two measurements at different distances. It is well-known that the forward operators in these cases are Fourier multipliers with so-called contrast transfer functions (CTF), and the zeros of the CTFs are responsible for general ill-posedness of the inverse problem. Our analysis exploits the regularizing effect on these zeros of the smoothness in Fourier space that results from the assumed support constraints.

The remainder of this paper is organized as follows: in §2, the mathematical model of X-ray phase contrast imaging is introduced and the considered inverse reconstruction problems, corresponding to different constraints and measurement setups, are motivated. Our principal stability results are stated in §2.4. §3, §4 and §5 contain the analysis for each of the inverse problems, including the proofs of the main results. In §6, we discuss implications of our findings and possible extensions.

2. Imaging problems and main results.

2.1. Physical model. An exemplary experimental setup for X-ray phase contrast imaging on a third generation synchrotron source (GINIX setup [39] at P10-beamline, DESY) is shown in Figure 1(a). We describe this imaging system by a standard wave-optical model as schematically visualized in Figure 1(b) [6,35]: an unknown sample is illuminated by an incident plane electromagnetic wave $\Psi_i(\mathbf{x}, z) = \exp(ikz)$, where $\mathbf{x} \in \mathbb{R}^2$ and $z \in \mathbb{R}$ denote the lateral- and axial coordinates, respectively. By scattering interaction, object information is encoded as a perturbation of the wave field $\Psi = \Psi_i + \Psi_s$ within the exit plane $z = 0$ of the probed sample. A detector measures the resulting near-field diffraction pattern (or hologram), given by the intensity $I(\mathbf{x}) = |\Psi(\mathbf{x}, d)|^2$ of the propagated wave fronts in some plane at finite distance $d > 0$ behind the object. The phase of the complex-valued field Ψ cannot be observed directly, yet *diffraction* partially encodes phase variations in the exit plane $z = 0$ into measurable intensities I at the detector.

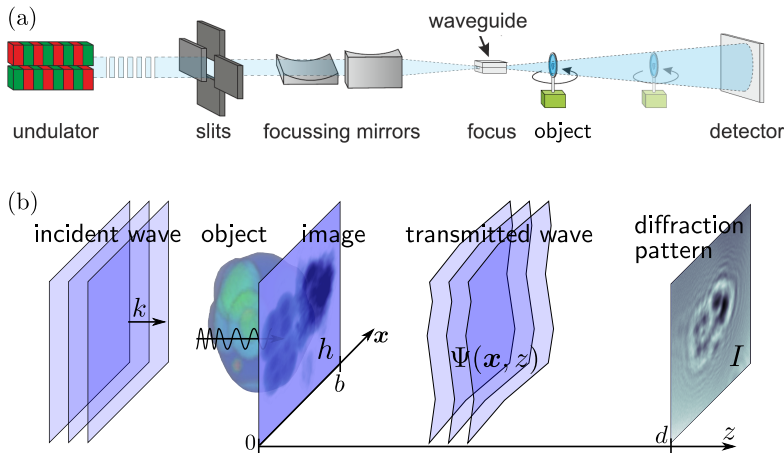


Fig. 1: Setup of propagation-based X-ray phase contrast imaging (inline holography). (a) Sketch of an experimental realization [26] (GINIX [39] at P10-beamline, DESY) (b) Physical model [25]: incident plane waves are scattered by an unknown sample, imprinting a phase- and absorption image $h = -i\phi - \mu$ upon the transmitted wave fronts $\Psi(\cdot, 0)$. The resulting near-field diffraction pattern (hologram) $I = |\Psi(\cdot, d)|^2$ is recorded at some distance $z = d$ behind the object. (plotted experimental data: hologram I and reconstructed image h of *d. radiodurans* bacteria).

In general, the above physical model is governed by the Helmholtz equation $\Delta\Psi + n^2k^2\Psi = 0$ in \mathbb{R}^3 , where the object gives rise to a spatially varying refractive index $n = 1 - \delta + i\beta$. In the hard X-ray regime of very large wavenumbers k , typical samples such as biological cells are often sufficiently thin and weakly interacting for the scattering to be well-approximated by geometrical optics [17, 32]. Within this approximation, the wave fronts $\Psi_z := \Psi(\cdot, z)$ in the exit plane are given by

$$(1) \quad \Psi_0 = \exp(h) \quad \text{with} \quad h = -i\phi - \mu = -ik \int_{\mathbb{R}} (\delta - i\beta) dz$$

Accordingly, the perturbed wave yields line integrals over δ and β along the incident z -direction, corresponding to a *projection image* of the sample in the form of phase

shifts ϕ and attenuation μ . In particular, (1) implies that the imprinted image h satisfies a *support constraint* $\text{supp}(h) \subset \Omega$ whenever the object is laterally finite, i.e. if $\delta(\mathbf{x}, z) = \beta(\mathbf{x}, z) = 0$ for all $z \in \mathbb{R}$, $\mathbf{x} \in \Omega$ outside some bounded domain $\Omega \subset \mathbb{R}^2$.

If $|\boldsymbol{\xi}| \ll k$ for all relevant spatial frequencies $\boldsymbol{\xi}$ of h , the total wave field will be of the form $\Psi(\mathbf{x}, z) = e^{ikz} \tilde{\Psi}(\mathbf{x}, z)$ with a slowly varying envelope $\tilde{\Psi}$ such that $e^{-ikz}(\partial_z^2 + k^2)\Psi \approx 2ik\partial_z \tilde{\Psi}$ by neglecting $\partial_z^2 \tilde{\Psi}$. This yields the one-way-, Schrödinger- or paraxial approximation

$$2ki\partial_z \tilde{\Psi} + \Delta_{\mathbf{x}} \tilde{\Psi} \approx 0$$

to the Helmholtz equation. Within this commonly used model, the free-space propagation of the wave fronts to the detector is described by the *Fresnel propagator* [32]:

$$(2) \quad \mathcal{D}(\Psi_0) := \exp(-ikd)\Psi_d = \mathcal{F}^{-1}(m_{\mathfrak{f}} \cdot \mathcal{F}(\Psi_0)) \quad m_{\mathfrak{f}}(\boldsymbol{\xi}) := \exp\left(\frac{-i|\boldsymbol{\xi}|^2}{2\mathfrak{f}}\right)$$

Here, \mathcal{F} is the Fourier transform and

$$(3) \quad \mathfrak{f} := \frac{kb^2}{d} \quad \text{or} \quad \mathfrak{f} := \frac{\mathfrak{f}}{2\pi}$$

denote the dimensionless *Fresnel number* of the setup. b is a physical length that corresponds to length 1 in dimensionless coordinates and will be chosen as the support diameter of the image h , see Figure 1(b). Usually \mathfrak{f} is referred to as Fresnel number, but this convention would lead to an abundance of 2π factors in our computations. Therefore, we will mostly use \mathfrak{f} with the notation (3) chosen in analogy to Planck's constant. \mathfrak{f} governs the impact of diffraction in the imaging setup, where smaller values correspond to stronger diffractive distortion of the propagating wave field. Typical values in experimental X-ray phase contrast setups are in the range $10 \leq \mathfrak{f} \leq 1000$.

By combination of (1) and (2), we find that the unknown object image h is related to the observable intensity data $I = |\Psi_d|^2$ by the nonlinear forward operator

$$(4) \quad I = F(h) := |\mathcal{D}(\exp(h))|^2 \quad \text{with} \quad h = -i\phi - \mu$$

We note that similar models apply to imaging with *electrons* [8, 22, 43] owing to the mathematical equivalence of the time-independent Schrödinger equation and the Helmholtz equation.

2.2. Weak object limit and principal inverse problem. By (4), the image h is in general complex-valued, whereas the intensity data I is real-valued. This suggests that the data is insufficient for unique and stable recovery of h [5, 30]. We analyze this question of ill-posedness within the commonly used *weak-object-approximation* [7, 13, 33, 35]: in the case of weak absorption $\mu \ll 1$ and slowly varying phase shifts ϕ , nonlinear terms in h can be neglected in (4) [42], giving

$$(5) \quad F(h) = 1 + Th + \mathcal{O}(h^2) \quad \text{with} \quad Th := 2\Re(\mathcal{D}(h)).$$

Here, \Re denotes the pointwise real-part and we have used that $\mathcal{D}(1) = 1$. Note that \mathcal{D} is unitary on $L^2(\mathbb{R}^m)$, so T defines a bounded \mathbb{R} -linear operator on $L^2(\mathbb{R}^m)$. Rather than by (5), T is more commonly written in terms of the phase shifts ϕ and absorption μ via sinusoidal *contrast transfer functions* (CTF) [12]:

$$(6) \quad T(-i\phi - \mu) = 2\mathcal{F}^{-1} \left(\sin\left(\frac{|\boldsymbol{\xi}|^2}{2\mathfrak{f}}\right) \mathcal{F}(\phi) - \cos\left(\frac{|\boldsymbol{\xi}|^2}{2\mathfrak{f}}\right) \mathcal{F}(\mu) \right).$$

Although the physical model of §2.1 leads to two-dimensional images h and holograms I , we will study the operator T in a more general \mathbb{R}^m -setting. This might allow application of our results to situations described by (quasi-) 1D-models and to *phase contrast tomography*, which can be interpreted as a 3D-imaging modality [19, 38]. As physically motivated in §2.1, we impose support constraints by assuming

$$(7) \quad h \in L^2_\Omega := \{h \in L^2(\mathbb{R}^m) : h|_{\mathbb{R}^m \setminus \Omega} = 0\} \quad \text{for some } \Omega \subset \mathbb{R}^m.$$

Moreover, we denote by $\|h\| := (\int_{\mathbb{R}^m} |h|^2 d\mathbf{x})^{1/2}$ the standard L^2 -norm in \mathbb{R}^m . The principal image reconstruction problem of this work then reads as follows:

INVERSE PROBLEM 1 (Phase contrast imaging of weak objects). *For a given support $\Omega \subset \mathbb{R}^m$, recover a complex-valued image $h \in L^2_\Omega$ from noisy intensity data*

$$I^\epsilon = 1 + Th + \epsilon \quad \text{with} \quad \|\epsilon\| \leq \epsilon.$$

2.3. Homogeneous and non-absorbing objects. It is often legitimate to assume that the object is *homogeneous* in the sense that phase shifts ϕ and attenuation μ are proportional, i.e.

$$(8) \quad h = -\mu - i\phi = -ie^{-i\alpha}\varphi$$

for some $\alpha \in [0; \pi)$ and a *real-valued* function $\varphi \in L^2(\mathbb{R}^m)$. Note that this includes the special case $\alpha = 0$ which corresponds to $\mu = 0$ and thus to a purely phase shifting, i.e. non-absorbing object, providing an excellent model for hard X-ray imaging of light-element samples. By plugging (8) into (6) and rearranging by trigonometric identities, we obtain a forward operator incorporating the *homogeneity constraint*:

$$(9) \quad S_\alpha : L^2(\mathbb{R}^m) \rightarrow L^2(\mathbb{R}^m), \quad \varphi \mapsto T(-ie^{-i\alpha}\varphi) = 2\mathcal{F}^{-1}(s_\alpha \cdot \mathcal{F}(\varphi)) \quad s_\alpha(\boldsymbol{\xi}) := \sin\left(\frac{|\boldsymbol{\xi}|^2}{2\mathfrak{f}} + \alpha\right)$$

Accordingly, the forward model reduces to a multiplication with the contrast transfer function s_α (CTF) in Fourier space [12, 42]. This makes the inversion of S_α significantly easier than that of T , which is why we state it as a second inverse problem:

INVERSE PROBLEM 2 (Phase contrast imaging of weak homogeneous objects). *For given $\Omega \subset \mathbb{R}^m$, recover a real-valued image $\varphi \in L^2_\Omega$ from noisy intensity data*

$$I^\epsilon = 1 + S_\alpha\varphi + \epsilon \quad \text{with} \quad \|\epsilon\| \leq \epsilon.$$

2.4. Stability estimates. The statement of **Inverse Problems 1** and **2** immediately raises the question whether these are uniquely solvable and whether the solution is *stable* with respect to noise ϵ . In order to illustrate the significance of this problem, we first recall some well-known facts on the derived inverse problems without assuming a support constraint, i.e. for $\Omega = \mathbb{R}^m$: as the null-space $\mathcal{N}(T) = \{i\mathcal{D}^{-1}(f) : f \in L^2(\mathbb{R}^m) \text{ real-valued}\}$ of the forward map $T : L^2(\mathbb{R}^m) \rightarrow L^2(\mathbb{R}^m)$ is huge, **Inverse Problem 1** is heavily non-unique in this setting. The operator S_α , on the other hand, is indeed injective so that **Inverse Problem 2** is uniquely solvable. However, the inversion of S_α is *ill-posed* since noise in Fourier-frequencies near the zeros of the CTF s_α is amplified by arbitrary factors in the reconstruction.

To our great surprise, imposing a support constraint with bounded Ω does not only rule out non-uniqueness (as proven in [25]), but even turns [Inverse Problem 1](#) into a *well-posed* problem: every admissible image $h \in L^2_\Omega$ gives rise to finite *contrast* $\|Th\| \geq C_{\text{IP1}} \|h\|$ in the observable data with some lower bound $C_{\text{IP1}} > 0$:

THEOREM 1 (Well-posedness and stability estimate for [Inverse Problem 1](#)). *Let the support-domain Ω be given by a stripe of width 1, without loss of generality $\Omega := [-1/2; 1/2] \times \mathbb{R}^{m-1}$. Then there exists a constant $C_{\text{IP1}}(\Omega, \mathfrak{f}) > 0$ such that*

$$(10) \quad \|Th\| \geq C_{\text{IP1}}(\Omega, \mathfrak{f}) \|h\| \quad \text{for all } h \in L^2_\Omega,$$

i.e. [Inverse Problem 1](#) is well-posed. The stability constant satisfies the estimate

$$(11) \quad C_{\text{IP1}}(\Omega, \mathfrak{f}) \geq (2\pi\mathfrak{f})^{\frac{1}{4}} \left(1 - \frac{3}{8\mathfrak{f}} + \mathcal{O}(\mathfrak{f}^{-2}) \right) \exp(-\mathfrak{f}/8).$$

[Theorem 1](#) is proven in §3 along with a characterization of the least stable modes, i.e. of the images h that induce least contrast under T . Notably, (10) implies $\|h\| \leq C_{\text{IP1}}(\Omega, \mathfrak{f})^{-1} \|Th\|$, ensuring finite amplification of data errors $\leq C_{\text{IP1}}(\Omega, \mathfrak{f})^{-1} \|\epsilon\|$ upon inversion of T and thus *stability* of the reconstruction of h from I^ϵ . By (11), however, the constant $C_{\text{IP1}}(\Omega, \mathfrak{f})$ decays (nearly) exponentially with increasing \mathfrak{f} so that [Theorem 1](#) hardly guarantees stability in any practical sense for Fresnel numbers $\mathfrak{f} \geq 100$. Fortunately, the stability estimate can be improved to algebraic decay with \mathfrak{f} in the case of [Inverse Problem 2](#), as shown in §4:

THEOREM 2 (Well-posedness and stability estimate for [Inverse Problem 2](#)). *Let the support-domain $\Omega := \{\mathbf{x} \in \mathbb{R}^m : |\mathbf{x}| \leq \frac{1}{2}\}$ be a ball of diameter 1. Then the stability constant $C_{\text{IP2}}(\Omega, \mathfrak{f}, \alpha) := \inf_{\varphi \in L^2_\Omega, \|\varphi\|=1} \|S_\alpha \varphi\|$ of [Inverse Problem 2](#) is bounded by*

$$(12) \quad C_{\text{IP2}}(\Omega, \mathfrak{f}, \alpha) \geq \max \left\{ \min \{c_1, c_2 \mathfrak{f}^{-1}\}, \min \{c_3 \alpha, c_4 \mathfrak{f}^{-\frac{1}{2}}\} \right\}$$

for some constants $c_j > 0$ that depend only on the dimension m . In particular, $C_{\text{IP2}}(\Omega, \mathfrak{f}, \alpha) = \mathcal{O}(\mathfrak{f}^{-1})$ for $\alpha = 0$ and $C_{\text{IP2}}(\Omega, \mathfrak{f}, \alpha) = \mathcal{O}(\mathfrak{f}^{-1/2})$ for $\alpha > 0$ as $\mathfrak{f} \rightarrow \infty$.

We recall that the physical lengthscale b underlying to the Fresnel number \mathfrak{f} in [Theorems 1](#) and [2](#) is the diameter of the support-domain Ω as the latter is taken to be unit length. Accordingly, the resulting stability constants $C_{\text{IP1}}, C_{\text{IP2}}$ are much smaller than 1 for typical values $10 \leq \mathfrak{f} \leq 1000$. Moreover, we emphasize that the stated results for [Inverse Problems 1](#) and [2](#) are both for reconstructions from a *single* diffraction pattern. Image recovery from *two* holograms recorded at different distances is treated in §5 as a corollary of the stability analysis of [Inverse Problem 2](#).

3. Stability analysis of [Inverse Problem 1](#).

3.1. Principal approach. We start our analysis with [Inverse Problem 1](#), corresponding to the recovery of general complex-valued images from a single hologram without homogeneity constraint. In order to understand its mathematical structure, it is instructive to rewrite the forward operator T in the form

$$(13) \quad \begin{aligned} Th &= 2\Re(\mathcal{D}(h)) = \mathcal{D}(h) + \overline{\mathcal{D}(h)} = \mathcal{D}(h) + \mathcal{F}^{-1}(m_{\mathfrak{f}}^{-1} \cdot \mathcal{F}(\bar{h})) \\ &= \mathcal{D}(h) + \mathcal{D}^{-1}(\bar{h}) \quad \text{for } h \in L^2(\mathbb{R}^m). \end{aligned}$$

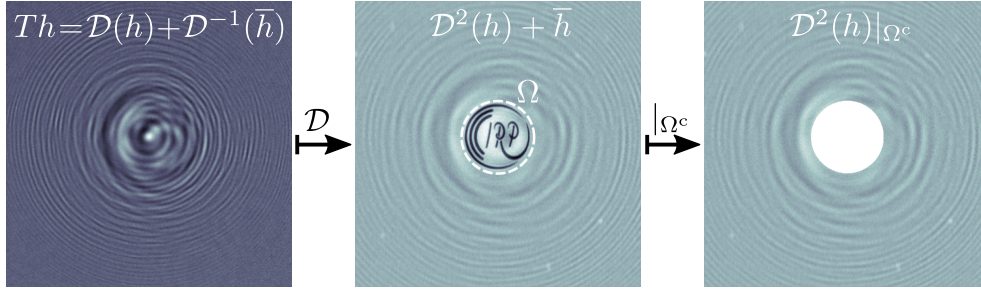


Fig. 2: Illustration of the principal idea for the stability analysis of [Inverse Problem 1](#). By applying the Fresnel propagator \mathcal{D} to data Th , the *twin-image* \bar{h} becomes sharp (*Gabor holography*, see logo in central panel). By restricting to the complement Ω^c of the support-domain $\Omega \supset \text{supp}(h)$, \bar{h} is eliminated and incomplete Fresnel data $\mathcal{D}^2(h)|_{\Omega^c}$ is obtained (right panel). Images show real parts of numerically computed fields from a hologram (left panel) recorded at GINIX [39], P10-beamline, DESY.

Here, the overbar denotes complex conjugation and we have used that the Fresnel propagation factor m_f is unitary. According to (13), the linearized contrast Th in the intensity data is given by a superposition of the propagated image $\mathcal{D}(h)$ and the *back-propagated twin-image* $\mathcal{D}^{-1}(\bar{h})$. Since \mathcal{D} is unitary, reconstructing h from one of these components *alone* would be straightforward. Solving [Inverse Problem 1](#) thus amounts to disentangling image and twin-image.

In order to separate these components, we propagate the near-field hologram Th by application of \mathcal{D} . By (13), this yields

$$(14) \quad \mathcal{D}Th = \mathcal{D}^2(h) + \bar{h}.$$

Accordingly, we recover the sharp twin-image \bar{h} up to perturbations originating from the doubly propagated image $\mathcal{D}^2(h)$. This is the principle of *Gabor holography* [10], which can be used as a *qualitative* image reconstruction technique [32] as illustrated in [Figure 2](#). Here, we follow this approach in a converse manner: rather than contenting ourselves with the perturbed twin-image \bar{h} , we exploit a *support constraint*

$$(15) \quad \text{supp}(h) = \overline{\{\mathbf{x} \in \mathbb{R}^m : h(\mathbf{x}) \neq 0\}} \subset \Omega$$

by restricting (14) to the complement of Ω . This yields

$$(16) \quad \mathcal{D}Th|_{\Omega^c} = \mathcal{D}^2(h)|_{\Omega^c} + \bar{h}|_{\Omega^c} = \mathcal{D}^2(h)|_{\Omega^c} \quad \text{for any } h \in L^2_{\Omega}.$$

By the proposed propagation-and-restriction procedure, the twin-image is thus completely eliminated from the data as sketched in [Figure 2](#). Note that the map $Th \mapsto \mathcal{D}(Th)|_{\Omega^c} = \mathcal{D}^2(h)|_{\Omega^c}$ is norm-decreasing in $L^2(\mathbb{R}^m)$. Hence, (16) implies that the solution of [Inverse Problem 1](#) is at most as ill-posed as the reconstruction from incomplete Fresnel data $\mathcal{D}^2(h)|_{\Omega^c}$. This reduction to a data completion problem is the principal idea of our stability analysis for [Inverse Problem 1](#).

3.2. Reduction to Fourier completion problem. In order to gain a simpler expression for the reduced data $\mathcal{D}^2(h)|_{\Omega^c}$ obtained in §3.1, we use an alternate form

of the Fresnel propagator \mathcal{D} . By application of the convolution theorem to (2), the following representation can be obtained (see e.g. [32]):

$$(17) \quad \mathcal{D}(h)(\mathbf{x}) = e^{-im\pi/4} \mathfrak{f}^{\frac{m}{2}} n_{\mathfrak{f}}(\mathbf{x}) \cdot \mathcal{F}(n_{\mathfrak{f}} \cdot h)(\mathfrak{f}\mathbf{x}), \quad n_{\mathfrak{f}}(\mathbf{x}) := \exp\left(\frac{i}{2}\mathfrak{f}|\mathbf{x}|^2\right)$$

for all $\mathbf{x} \in \mathbb{R}^m$. (17) reveals that - up to pointwise multiplications with the unitary factor $n_{\mathfrak{f}}$ and rescaling - \mathcal{D} may be written as a Fourier transform. Combined with the approach outlined in §3.1, this allows to identify stability of **Inverse Problem 1** with the reconstruction of a function from *incomplete Fourier data*:

THEOREM 3 (Reduction to Fourier data completion problem). *Within the setting of **Inverse Problem 1**, let $\Omega_{\mathfrak{f}} := \{(\mathfrak{f}/2)\mathbf{x} : \mathbf{x} \in \Omega\}$ for arbitrary $\Omega \subset \mathbb{R}^m$. Then*

$$(18) \quad \|Th\| \geq \|\mathcal{F}(n_{\mathfrak{f}}^{1/2} \cdot h)|_{\Omega_{\mathfrak{f}}^c}\| \quad \text{for all } h \in L_{\Omega}^2$$

where $n_{\mathfrak{f}}^{1/2}(\mathbf{x}) = \exp(i\mathfrak{f}|\mathbf{x}|^2/4)$. In particular, we have the relative stability estimate

$$(19) \quad C_{\text{IP1}}(\Omega, \mathfrak{f}) = \inf_{h \in L_{\Omega}^2, \|h\|=1} \|Th\| \geq \inf_{h \in L_{\Omega}^2, \|h\|=1} \|\mathcal{F}(h)|_{\Omega_{\mathfrak{f}}^c}\|$$

Proof. \mathcal{D} is unitary and the restriction to $\Omega^c \subset \mathbb{R}^m$ defines an orthogonal projection in $L^2(\mathbb{R}^m)$. Hence, (16) implies the estimate

$$(20) \quad \|Th\| = \|\mathcal{D}Th\| \geq \|\mathcal{D}Th|_{\Omega^c}\| = \|\mathcal{D}^2(h)|_{\Omega^c}\| \quad \text{for any } h \in L_{\Omega}^2.$$

By (2), \mathcal{D}^2 is again a Fresnel propagator, yet to the Fresnel number $\mathfrak{f}/2$. Accordingly, employing the alternative form (17) and exploiting that $|e^{-im\pi/4} n_{\mathfrak{f}}^{1/2}| \equiv 1$ gives

$$(21) \quad \|\mathcal{D}^2(h)|_{\Omega^c}\| = \left(\frac{1}{2}\mathfrak{f}\right)^{\frac{m}{2}} \left\| \mathcal{F}(n_{\mathfrak{f}}^{1/2} \cdot h)\left(\frac{1}{2}\mathfrak{f}\cdot\right)|_{\Omega^c} \right\|.$$

Introducing new coordinates $\boldsymbol{\xi} := (\mathfrak{f}/2)\mathbf{x}$ and using that $\Omega_{\mathfrak{f}}^c = (\mathfrak{f}/2) \cdot \Omega^c$ holds by definition, this expression can be simplified to

$$(22) \quad \begin{aligned} \|\mathcal{D}^2(h)|_{\Omega^c}\|^2 &= \left(\frac{1}{2}\mathfrak{f}\right)^m \int_{\Omega^c} |\mathcal{F}(n_{\mathfrak{f}}^{1/2} \cdot h)\left(\frac{1}{2}\mathfrak{f}\mathbf{x}\right)|^2 d\mathbf{x} \\ &= \int_{\Omega_{\mathfrak{f}}^c} |\mathcal{F}(n_{\mathfrak{f}}^{1/2} \cdot h)(\boldsymbol{\xi})|^2 d\boldsymbol{\xi} = \left\| \mathcal{F}(n_{\mathfrak{f}}^{1/2} \cdot h)|_{\Omega_{\mathfrak{f}}^c} \right\|^2. \end{aligned}$$

Combining (20) and (22) yields the first assertion (18). The second estimate (19) then follows from the fact that the map $h \mapsto n_{\mathfrak{f}}^{1/2} \cdot h$ is isometric and bijective on L_{Ω}^2 . \square

Theorem 3 states that the solution of **Inverse Problem 1** is *at least as stable* as the reconstruction of an L^2 -function f with support in $\Omega \subset \mathbb{R}^m$ from incomplete Fourier measurements $\mathcal{F}(f)|_{\Omega_{\mathfrak{f}}}$. For compact Ω , the latter Fourier completion problem can be shown to be unique and even *well-posed* by employing an uncertainty principle for the 1D-Fourier transform derived by Nazarov [29] (see [14] for an English proof and [16] for its multidimensional generalization). Rather than following this approach for general support shapes, however, we will restrict to the special case of rectangular support-domains Ω . This will enable a more explicit characterization of the dependence of C_{IP1} on the Fresnel number \mathfrak{f} via **Theorem 3** as well as additional insights concerning the nature of the least stable modes of the forward operator T .

3.3. Stability result for stripe-shaped supports. In the following, we restrict to the simple case of a stripe-shaped support-domain $\Omega \subset \mathbb{R}^m$ as considered in [Theorem 1](#). Note that the forward operator T is rotationally- and translationally invariant as is the Fresnel propagator \mathcal{D} . Hence, it is sufficient to consider domains of the form $\Omega := [-b/2; b/2] \times \mathbb{R}^{m-1}$. Moreover, b can be set to 1 which means that we define the Fresnel number \mathfrak{f} with respect to the support diameter. Accordingly, we may indeed restrict to the special case $\Omega := [-1/2; 1/2] \times \mathbb{R}^{m-1}$ as done in [Theorem 1](#) without loss of generality.

Now we can employ the characterization of the stability constant in [Theorem 3](#) for this special domain. We define $I := [-1/2; 1/2]$ and $I_{\mathfrak{f}} := [-\mathfrak{f}/4; \mathfrak{f}/4]$ for notational convenience. Recall that the m -dimensional Fourier transform $\mathcal{F}^{(m)}$ is a tensor product of one-dimensional Fourier transforms $\mathcal{F}^{(1)}$ applied along the different coordinate dimensions, i.e. $\mathcal{F}^{(m)} = \mathcal{F}^{(1)} \otimes \dots \otimes \mathcal{F}^{(1)}$. Owing to the cartesian product structure of $\Omega = I \times \mathbb{R}^{m-1}$ and $\Omega_{\mathfrak{f}}^c = I_{\mathfrak{f}}^c \times \mathbb{R}^{m-1}$, the restricted Fourier transforms

$$(23) \quad \mathcal{F}_{\Omega, \Omega_{\mathfrak{f}}^c}^{(m)} : L_{\Omega}^2 \rightarrow L_{\Omega_{\mathfrak{f}}^c}^2; h \mapsto (\mathcal{F}^{(m)}h)|_{\Omega_{\mathfrak{f}}^c}, \quad \mathcal{F}_{I, I_{\mathfrak{f}}^c}^{(1)} : L_I^2 \rightarrow L_{I_{\mathfrak{f}}^c}^2; h \mapsto (\mathcal{F}^{(1)}h)|_{I_{\mathfrak{f}}^c},$$

are likewise related by $\mathcal{F}_{\Omega, \Omega_{\mathfrak{f}}^c}^{(m)} = \mathcal{F}_{I, I_{\mathfrak{f}}^c}^{(1)} \otimes \mathcal{F}^{(1)} \otimes \dots \otimes \mathcal{F}^{(1)}$. Applying this relation to the stability estimate in [\(19\)](#) and exploiting unitarity of the Fourier transform yields

$$(24) \quad \begin{aligned} C_{\text{IP1}}(\Omega, \mathfrak{f}) &= \inf_{h \in L_{\Omega}^2, \|h\|=1} \|\mathcal{F}_{\Omega, \Omega_{\mathfrak{f}}^c}^{(m)} h\| = \inf_{h \in L_I^2, \|h\|=1} \|\mathcal{F}_{I, I_{\mathfrak{f}}^c}^{(1)} h\| \\ &= \left(1 - \sup_{h \in L_I^2, \|h\|=1} \|\mathcal{F}^{(1)}(h)|_{I_{\mathfrak{f}}}\|^2 \right)^{1/2}. \end{aligned}$$

We thus need to estimate the norm of the 1D-operator $\mathcal{F}_{\mathfrak{f}} : L_I^2 \rightarrow L_{I_{\mathfrak{f}}}^2; h \mapsto \mathcal{F}^{(1)}(h)|_{I_{\mathfrak{f}}}$. This is achieved by explicit computation of the operator $\mathcal{F}_{\mathfrak{f}}^* \mathcal{F}_{\mathfrak{f}}$ ($\mathcal{F}_{\mathfrak{f}}^*$: adjoint of $\mathcal{F}_{\mathfrak{f}}$), which turns out to be part of a well-studied family of compact and self-adjoint integral operators. Their eigenfunctions are known as prolate spheroidal wave functions, and the eigenpairs have been studied for example in [\[40, 41\]](#). By applying these known results we obtain the following theorem:

THEOREM 4 (Spectral characterization of $\mathcal{F}_{\mathfrak{f}}^* \mathcal{F}_{\mathfrak{f}}$). *Let $\mathcal{F}_{\mathfrak{f}}$ defined by [\(23\)](#). Then*

$$(25) \quad \mathcal{F}_{\mathfrak{f}}^* \mathcal{F}_{\mathfrak{f}}(f) \left(\frac{x}{2} \right) = \int_{-1}^1 \frac{\sin(c(x-y))}{\pi(x-y)} f \left(\frac{y}{2} \right) dy \quad \text{with} \quad c := \mathfrak{f}/8.$$

for all $h \in L_I^2$ and $x \in [-1; 1]$, and $\mathcal{F}_{\mathfrak{f}}^* \mathcal{F}_{\mathfrak{f}}$ is compact. The eigenvalues $\{\lambda_{c,j}\}_{j \in \mathbb{N}_0} \subset \mathbb{R}_+$ and associated eigenfunctions $\{\psi_{c,j}\}_{j \in \mathbb{N}_0} \subset L_I^2$ of $\mathcal{F}_{\mathfrak{f}}^* \mathcal{F}_{\mathfrak{f}}$ thus coincide with those in [\[40, 41\]](#). In particular, all eigenvalues $\lambda_{c,0} > \lambda_{c,1} > \dots$ have multiplicity one, and the $\psi_{c,j}$ may be chosen to form an orthonormal basis of L_I^2 . Moreover, $\lambda_{c,0} < 1$ holds true and, for fixed $j \in \mathbb{N}_0$ and $\mathfrak{f} \rightarrow \infty$, $\lambda_{c,j}$ has the asymptotic expansion

$$(26) \quad 1 - \lambda_{c,j} = \frac{(2\pi)^{\frac{1}{2}} \mathfrak{f}^{j+\frac{1}{2}}}{j!} \left(1 - \frac{6j^2 - 2j + 3}{4\mathfrak{f}} + \mathcal{O}\left(\frac{1}{\mathfrak{f}^2}\right) \right) \exp(-\mathfrak{f}/4).$$

Proof. The restriction to the interval $I_{\mathfrak{f}} = [-\mathfrak{f}/4; \mathfrak{f}/4]$ can be written in the form of a multiplication with its indicator function $\mathbf{1}_{I_{\mathfrak{f}}}$. By the convolution theorem, we thus obtain for all $h \in L_I^2$, $x \in [-1; 1]$

$$\begin{aligned} \mathcal{F}_f^* \mathcal{F}_f(h) \left(\frac{x}{2} \right) &= \mathcal{F}^{-1}(\mathbf{1}_{I_f} \cdot \mathcal{F}(h)) \left(\frac{x}{2} \right) = (2\pi)^{-\frac{1}{2}} \mathcal{F}^{-1}(\mathbf{1}_{I_f}) * h \left(\frac{x}{2} \right) \\ &= \frac{1}{2\pi} \int_{-1/2}^{1/2} \frac{2 \sin\left(\frac{f}{4}\left(\frac{x}{2} - y\right)\right)}{\frac{1}{2}x - y} f(y) \, dy = \int_1^1 \frac{\sin(c(x-y))}{\pi(x-y)} f\left(\frac{y}{2}\right) \, dy. \end{aligned}$$

The spectral characterization of the resulting integral operators in [40, 41] directly yields the claimed properties of the eigensystem $\{(\lambda_{c,j}, \psi_{c,j})\}_{j \in \mathbb{N}_0}$ of $\mathcal{F}_f^* \mathcal{F}_f$. In particular, the asymptotic expansion (26) is an analogue of the formula [40, eq. (2)].

Since \mathcal{F}_f is a restriction of the Fourier transform, we have $\|\mathcal{F}_f\| \leq \|\mathcal{F}\| = 1$. Hence, the principal eigenvalue of $\mathcal{F}_f^* \mathcal{F}_f$ must satisfy $\lambda_{c,0} \leq 1$. If $\lambda_{c,0} = 1$ then

$$\left\| \mathcal{F}(\psi_{c,0})|_{I_f} \right\|^2 = \|\mathcal{F}(\psi_{c,0})\|^2 - \|\mathcal{F}(\psi_{c,0})|_{I_f}\|^2 = \|\psi_{c,0}\|^2 - \lambda_{c,0} \|\psi_{c,0}\|^2 = 0,$$

i.e. $\mathcal{F}(\psi_{c,0})$ would have to vanish outside the interval I_f . However, as $\psi_{c,0}$ is compactly supported, $\mathcal{F}(\psi_{c,0})$ is an entire function and thus vanishes identically if $\mathcal{F}(\psi_{c,0})|_{I_f} = 0$. This is impossible since $\psi_{c,0}$ is an eigenfunction. Hence, $\lambda_{c,0} < 1$ must hold true. \square

We emphasize the nontrivial dependence of both the eigenvalues $\lambda_{c,j}$ and the eigenfunctions $\psi_{c,j}$ on the parameter $c = f/8$. For convenience, however, we will suppress the subscript c in the following. **Theorem 4** constitutes the final ingredient which is needed to prove the sought stability result for **Inverse Problem 1**:

Proof of Theorem 1. According to the characterization of the stability constant in (24), $C_{\text{IP1}}(\Omega, f)$ can be expressed in terms of the operator norm of \mathcal{F}_f . Since $\mathcal{F}_f^* \mathcal{F}_f$ is compact with principal eigenvalue $\lambda_0 < 1$ and orthonormal eigenfunctions $\{\psi_j\}_{j \in \mathbb{N}_0}$ as characterized in **Theorem 4**, we have

$$\|\mathcal{F}_f\|^2 = \|\mathcal{F}_f^* \mathcal{F}_f\| = \sup_{j \in \mathbb{N}_0} \|\mathcal{F}_f^* \mathcal{F}_f \psi_j\| = \sup_{j \in \mathbb{N}_0} \lambda_j = \lambda_0$$

By (24), this implies $C_{\text{IP1}}(\Omega, f)^2 = 1 - \lambda_0 > 0$, i.e. *well-posedness* of **Inverse Problem 1**. Setting $j = 0$ in (26) yields the asymptotic characterization (11). \square

3.4. Characterization of the least stable modes. So far, we have not exploited the full potential of the reduction to a Fourier data completion problem in **Theorem 3** yet: only the characterization of the stability constant (19), i.e. of the *worst-case-stability*, has been used in the proof of **Theorem 1**. Notably however, the more general estimate (18) even bounds the contrast $\|Th\|$ attained by *individual images* h with respect to the corresponding incomplete Fourier data $\mathcal{F}(n_f^{1/2} \cdot h)|_{\Omega_f^c}$. This enables a precise prediction of the reconstruction stability for different image modes in **Inverse Problem 1** beyond the universal lower bound proven in **Theorem 1**.

In order to avoid notational difficulties in the argument, we do the analysis for a box-shaped support-domain $\Omega := [-1/2; 1/2]^m = I^m$. Owing to the simple Cartesian geometry, the results obtained for a stripe support are easily generalized to this case, including a characterization of the stability of individual modes. We define m -dimensional prolate spheroidal wave functions as the tensor product

$$(27) \quad \psi_j(\mathbf{x}) := (\psi_{j_1} \otimes \dots \otimes \psi_{j_m})(\mathbf{x}) := \prod_{j=1}^m \psi_j(x_j) \quad \text{for } \mathbf{j} = (j_1, \dots, j_m) \in \mathbb{N}_0^m.$$

Moreover, let $\langle f, g \rangle := \int_{\Omega} f(\mathbf{x}) \overline{g(\mathbf{x})} \, d\mathbf{x}$ for $h_1, h_2 \in L^2_{\Omega}$ denote usual L^2 -inner product. With this notation, we obtain the following modal stability estimates:

THEOREM 5 (Stability of individual modes in [Inverse Problem 1](#)). *Let $\Omega = I^m$ and let $\{(\lambda_j, \psi_j)\}_{j \in \mathbb{N}_0}$ denote the eigenvalue decomposition of $\mathcal{F}_f^* \mathcal{F}_f$ in [Theorem 4](#). Moreover, define $\phi_j := n_f^{-1/2} \cdot \psi_j$ for all multi-indices $\mathbf{j} \in \mathbb{N}_0^m$. Then $\{\phi_j\}_{j \in \mathbb{N}_0^m}$ is an orthonormal basis of L_Ω^2 , and with $c_{\text{IP1}, \mathbf{j}} := (1 - \prod_{l=1}^m \lambda_{j_l})^{1/2}$ we have*

$$(28) \quad \|Th\|^2 \geq \sum_{\mathbf{j} \in \mathbb{N}_0^m} c_{\text{IP1}, \mathbf{j}}^2 |\langle h, \phi_j \rangle|^2 \quad \text{for any } h = \sum_{\mathbf{j} \in \mathbb{N}_0^m} \langle h, \phi_j \rangle \phi_j \in L_\Omega^2.$$

Proof. As $\{\psi_j\}_{j \in \mathbb{N}_0}$ is an orthonormal basis of L_I^2 , the tensor products $\psi_{\mathbf{j}} = \psi_{j_1} \otimes \dots \otimes \psi_{j_m}$ form an orthonormal basis of L_Ω^2 with $\Omega = I^m$. Since $n_f^{-1/2}$ is unitary, the same is true for $\{\phi_j\}_{j \in \mathbb{N}_0^m}$ so that any $h \in L_\Omega^2$ can be written as $h = \sum_{\mathbf{j} \in \mathbb{N}_0^m} a_j \phi_j$ with $a_j := \langle h, \phi_j \rangle$. By the tensor product structure of ψ_j and $\mathcal{F}^{(m)}$, we further have

$$\begin{aligned} \mathcal{F}^{(m)}(n_f^{1/2} \cdot \phi_j)|_{\Omega_f} &= \mathcal{F}^{(m)}(\psi_j)|_{I_f^m} = (\mathcal{F}^{(1)}\psi_{j_1})|_{I_f} \otimes \dots \otimes (\mathcal{F}^{(1)}\psi_{j_m})|_{I_f} \\ &= \mathcal{F}_f \psi_{j_1} \otimes \dots \otimes \mathcal{F}_f \psi_{j_m} \end{aligned}$$

for all $\mathbf{j} = (j_1, \dots, j_m) \in \mathbb{N}_0$. As the ψ_l are eigenfunctions of the 1D-map $\mathcal{F}_f^* \mathcal{F}_f$ to the eigenvalues λ_l (see [Theorem 4](#)), the above relation implies

$$(29) \quad \begin{aligned} &\left\langle \mathcal{F}(n_f^{1/2} \cdot \phi_j)|_{\Omega_f}, \mathcal{F}(n_f^{1/2} \cdot \phi_{\mathbf{k}})|_{\Omega_f} \right\rangle \\ &= \prod_{l=1}^m \langle \mathcal{F}_f^* \mathcal{F}_f(\psi_{j_l}), \psi_{k_l} \rangle = \prod_{l=1}^m \lambda_{j_l} \langle \psi_{j_l}, \psi_{k_l} \rangle = \delta_{\mathbf{j}\mathbf{k}} \prod_{l=1}^m \lambda_{j_l} = \delta_{\mathbf{j}\mathbf{k}} (1 - c_{\text{IP1}, \mathbf{j}}^2) \end{aligned}$$

for all $\mathbf{j}, \mathbf{k} \in \mathbb{N}_0^m$ where $\delta_{\mathbf{j}\mathbf{k}} \in \{0, 1\}$ is the multidimensional Kronecker-symbol. Using the principal bound (18) from [Theorem 3](#), unitarity of \mathcal{F} and (29) finally gives

$$\begin{aligned} \|Th\|^2 &\geq \left\| \mathcal{F}(n_f^{1/2} \cdot h)|_{\Omega_f} \right\|^2 = \|h\|^2 - \left\| \mathcal{F}(n_f^{1/2} \cdot h)|_{\Omega_f} \right\|^2 \\ &= \sum_{\mathbf{j} \in \mathbb{N}_0^m} |a_j|^2 - \sum_{\mathbf{j}, \mathbf{k} \in \mathbb{N}_0^m} a_j \overline{a_{\mathbf{k}}} \left\langle \mathcal{F}(n_f^{1/2} \cdot \phi_j)|_{\Omega_f}, \mathcal{F}(n_f^{1/2} \cdot \phi_{\mathbf{k}})|_{\Omega_f} \right\rangle = \sum_{\mathbf{j} \in \mathbb{N}_0^m} c_{\text{IP1}, \mathbf{j}}^2 |a_j|^2 \square \end{aligned}$$

In [Theorem 5](#) we obtain *individual* stability constants $c_{\text{IP1}, \mathbf{j}}$ such that each of the constructed orthonormal basis modes ϕ_j attains data contrast $\|T\phi_j\| \geq c_{\text{IP1}, \mathbf{j}}$. As the sequence of eigenvalues $\{\lambda_j\}_{k \in \mathbb{N}_0}$ in [Theorem 4](#) is strictly decreasing, it is readily seen that stability *increases* with the multi-index \mathbf{j} , i.e.

$$(30) \quad c_{\text{IP1}, \mathbf{k}} > c_{\text{IP1}, \mathbf{j}} \quad \text{if } \mathbf{k} \neq \mathbf{j}, k_l \geq j_l \quad \text{for all } l = 1, \dots, m.$$

According to [Theorem 5](#), the least stable modes are thus exactly the basis functions ϕ_j of (componentwise) small multi-index \mathbf{j} , which are given by prolate spheroidal wave functions $\psi_{\mathbf{j}} = \psi_{j_1} \otimes \dots \otimes \psi_{j_m}$, modulated by the Fresnel factor $n_f^{-1/2}$. Details on the shape of the ψ_j in turn are readily available, see e.g. [40]. In particular, the index j can be interpreted as a *frequency* since ψ_j is smooth and real-valued with exactly j zeros and $j+1$ extrema within the interval $(-1/2; 1/2)$. By extending this observation to the ϕ_j we deduce the nature of the least stable modes in [Inverse Problem 1](#):

COROLLARY 6 (Least stable modes in [Inverse Problem 1](#)). *The least stable modes in [Inverse Problem 1](#) for $\Omega = [-1/2; 1/2]^m$ are low-frequency prolate spheroidal wave functions modulated by the Fresnel-factor $n_f^{-1/2}(\mathbf{x}) = \exp(-i\mathbf{j}|\mathbf{x}|^2/4)$.*

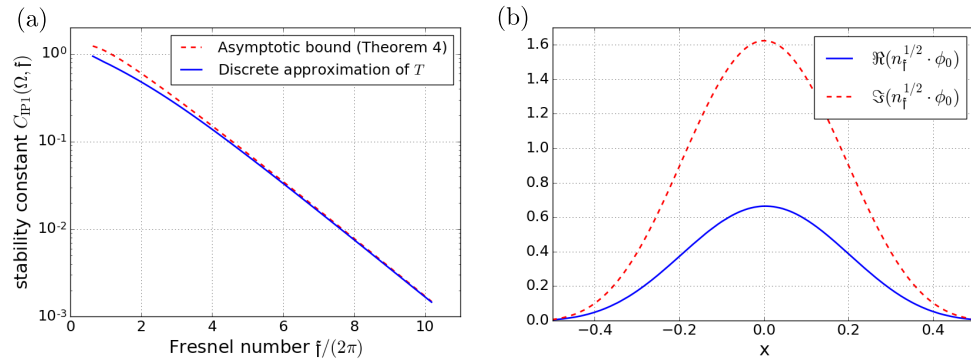


Fig. 3: Numerical validation of the stability analysis for **Inverse Problem 1**.

(a) Comparison of the analytical bound (11) for the stability constant C_{IP1} (red-dashed line) to numerical computations of the smallest singular value of T (blue-solid). (b) Numerically computed least stable singular mode ϕ_0 for $\mathfrak{f} = \mathfrak{f}/(2\pi) = 10$. The plotted modulation with $n_{\mathfrak{f}}^{1/2}$ reveals a unimodal structure as predicted by **Theorem 5**.

3.5. Numerical Validation. We return to the starting point of our stability analysis, namely the reduction to a Fourier data completion problem via the principal estimate (18). The question whether or not the derived stability bounds in **Theorem 1** and **Theorem 5** are *optimal* (or at least close to) crucially depends on the sharpness of this inequality. In the following we investigate this remaining issue numerically.

To this end, we approximate the stability bound $C_{IP1}(\Omega, \mathfrak{f})$ by computing the smallest singular value of a discretized forward operator T in $m = 1$ dimensions. The Fresnel propagator is approximated by fast Fourier transforms on a 1D-grid of 512^2 equidistant points, where the central 512 grid points form the supporting interval $\Omega = [-1/2; 1/2]$. We compute the smallest singular value of T via a power method for Fresnel numbers $\mathfrak{f} \in [1; 10]$. These numerical results for the complete, yet discretized forward operator, are compared to the asymptotic stability bound (11) in **Theorem 1**, neglecting the $\mathcal{O}(\mathfrak{f}^{-2})$ -contributions. The different predictions for the stability constant $C_{IP1}(\Omega, \mathfrak{f})$ are plotted in **Figure 3(a)**.

The semilogarithmic plot shows excellent agreement between the analytical bound (11) and the numerical approximation in the asymptotic limit $\mathfrak{f} \rightarrow \infty$. This indicates that our stability analysis, based on the potentially lossy estimate (18), is surprisingly sharp. Accordingly, one might expect that also the corresponding least stable modes $\phi_{\mathfrak{f}}$ are well-characterized by **Theorem 5**. This is supported by the simulation results: **Figure 3(b)** exemplarily plots the numerically computed mode ϕ_0 to the minimum singular value of T for $\mathfrak{f} = \mathfrak{f}/(2\pi) = 10$. According to **Theorem 1**, the plotted product with the factor $n_{\mathfrak{f}}^{1/2}$ should yield the zeroth order prolate spheroidal wave function ψ_0 . This is confirmed by the smooth unimodal profiles obtained in **Figure 3(b)**.

4. Stability analysis of Inverse Problem 2. The aim of this section is to prove **Theorem 2**, establishing *algebraic* rates of the stability constant $C_{IP2}(\Omega, \mathfrak{f}) \gtrsim \mathfrak{f}^{-1}$ under a homogeneity constraint for the imaged object.

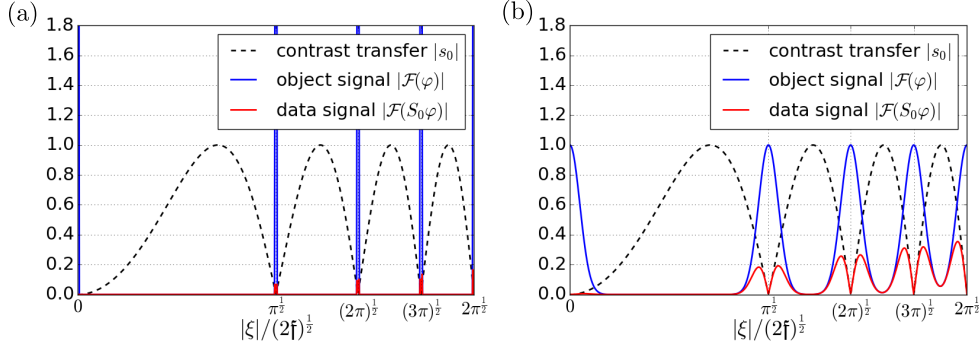


Fig. 4: Illustration of the principal argument for stability of **Inverse Problem 2**: the black-dashed line plots the radially symmetric contrast transfer function s_α for $\alpha = 0$. Blue and red solid lines show examples of Fourier space signals of objects φ and their images under the forward operator S_α , respectively.

(a) General images $\varphi \in L^2(\mathbb{R}^m)$: $\mathcal{F}(\varphi)$ may be arbitrarily peaked at the zeros of s_α
 (b) Support constraint $\varphi \in L^2_\Omega$: $\mathcal{F}(\varphi)$ is smooth and has finitely sharp peaks, which ensures minimum data contrast $\|\mathcal{F}(S_\alpha\varphi)\| \geq C_{\text{IP2}} \|\mathcal{F}(\varphi)\|$

4.1. Preparations and Fourier domain splitting. Throughout this section, let $\varphi \in L^2(\mathbb{R}^m)$ and let $\hat{\varphi} := \mathcal{F}(\varphi)$ denote its Fourier transform. Recall from definition (9) that the operator S_α denotes multiplication with $2s_\alpha(\boldsymbol{\xi}) = 2 \sin(|\boldsymbol{\xi}|^2/(2f) + \alpha)$ in the Fourier domain, and hence

$$(31) \quad \|S_\alpha\varphi\| = \|\mathcal{F}S_\alpha\varphi\| = 2 \|s_\alpha \cdot \hat{\varphi}\|.$$

According to (31), the images φ attaining low contrast, i.e. small $\|S_\alpha\varphi\|$, are exactly those for which $\hat{\varphi}$ is concentrated about the zero-manifolds of the CTF s_α . As signals $\hat{\varphi} \in L^2(\mathbb{R}^m)$ may be arbitrarily sharply peaked about these manifolds of zero contrast, **Inverse Problem 2** is ill-posed for general images $\varphi \in L^2(\mathbb{R}^m)$.

Now, we additionally assume a support constraint $\varphi \in L^2_\Omega$ for $\Omega := \overline{B(0, R)}$. Why does this constraint ensure well-posedness in the light of the problematic CTF-zeros? The explanation lies in the well-known fact that a compact support in real-space implies \mathcal{C}^∞ -smoothness (indeed analyticity) of the Fourier transform with norm-bounds on the derivatives in terms of the support size R . Owing to this regularity, $\hat{\varphi}$ may not be arbitrarily concentrated about the zero-manifolds of s_α , which enables stability as illustrated in **Figure 4**. The following lemma quantifies the smoothness of $\hat{\varphi}$ in a suitable form for the subsequent analysis:

LEMMA 7. *Let $g \in L^2_\Omega$ with support in $\Omega = \overline{B(0, R)}$ and Fourier transform $\hat{g} := \mathcal{F}(g)$. Let Δ be the Laplacian on \mathbb{R}^m . Then we have for any measurable set $B \subset \mathbb{R}^m$*

$$(32) \quad \int_B -\Delta|\hat{g}|^2 \, d\boldsymbol{\xi} \leq 2R^2 \|g\|^2.$$

Proof. The compact support of g implies infinite smoothness of $\hat{g} = \mathcal{F}(g)$. Using

the identity $-\Delta \mathcal{F}(g) = \mathcal{F}(|\mathbf{x}|^2 g)$ and Cauchy-Schwarz's inequality we obtain

$$\begin{aligned} \int_B -\Delta |\hat{g}|^2 \, d\boldsymbol{\xi} &= -2 \int_B \left(|\nabla \hat{g}|^2 + \Re(\bar{\hat{g}} \cdot \Delta \hat{g}) \right) \, d\boldsymbol{\xi} \leq 2 \left| \int_B \bar{\hat{g}} \cdot \mathcal{F}(|\mathbf{x}|^2 g) \, d\boldsymbol{\xi} \right| \\ &\leq 2 \|\hat{g}\|_B \|\mathcal{F}(|\mathbf{x}|^2 g)\|_B \leq 2 \|\hat{g}\| \|\mathcal{F}(|\mathbf{x}|^2 g)\| \leq 2 \|g\| \|\mathbf{x}|^2 g\|. \end{aligned}$$

As g vanishes outside $\overline{B(0, R)}$, we further have $\|\mathbf{x}|^2 g\| \leq R^2 \|g\|$. \square

Note that Lemma 7 can be interpreted as an *uncertainty principle*: a bound for the derivative $-\Delta |\mathcal{F}(g)|^2$, limiting the sharpness of features in Fourier space, arises from the confinement $\text{supp}(g) \subset \overline{B(0, R)}$ of the corresponding real-space signal g .

For a quantitative analysis, we decompose the norm on the right-hand side of (31) into stable bulk integrals and potentially unstable parts about the CTF-zeros by cutting out the subdomain $D_\varepsilon := \{\boldsymbol{\xi} \in \mathbb{R}^m : |s_\alpha(\boldsymbol{\xi})| \geq \sin(\varepsilon)\}$ for some $0 < \varepsilon \leq \pi/6$:

$$(33) \quad \|s_\alpha \cdot \hat{\varphi}\|^2 = \underbrace{\int_{D_\varepsilon} s_\alpha(\boldsymbol{\xi})^2 |\hat{\varphi}(\boldsymbol{\xi})|^2 \, d\boldsymbol{\xi}}_{=: J_\varepsilon} + \sum_{j=0}^{\infty} \underbrace{\int_{B_j} s_\alpha(\boldsymbol{\xi})^2 |\hat{\varphi}(\boldsymbol{\xi})|^2 \, d\boldsymbol{\xi}}_{=: J_j}$$

Here, the B_j denote the annular connected components of $\mathbb{R}^m \setminus D_\varepsilon$ about the j -th zero-manifold of s_α at radius $\xi_j := (2\mathbf{f})^{\frac{1}{2}}(j\pi - \alpha)^{\frac{1}{2}}$, i.e.

$$(34) \quad \begin{aligned} B_j &= \{\boldsymbol{\xi} \in \mathbb{R}^m : |\boldsymbol{\xi}| \in (b_{j-}; b_{j+})\}, \quad b_{j\pm} := (\xi_j^2 \pm 2\mathbf{f}\varepsilon)^{\frac{1}{2}} \quad \text{for } j \in \mathbb{N} \\ B_0 &= \{\boldsymbol{\xi} \in \mathbb{R}^m : |\boldsymbol{\xi}| < b_0\}, \quad b_0 := (2\mathbf{f})^{\frac{1}{2}} \max(\varepsilon - \alpha, 0)^{\frac{1}{2}}. \end{aligned}$$

Note that the constructed Fourier domain splitting is disjoint, i.e. $\mathbb{R}^m = (\bigsqcup_{j=0}^{\infty} B_j) \sqcup D_\varepsilon$. From the definition of the domain D_ε , it immediately follows that

$$(35) \quad J_\varepsilon \geq \sin(\varepsilon) \|\hat{\varphi}|_{D_\varepsilon}\|.$$

Hence, what remains to be done is to derive bounds for the sub-integrals J_j around the zero-manifolds of s_α and to choose ε to balance the contributions in (33).

4.2. Estimate for the central CTF-minimum. We first consider the ball-shaped domain B_0 , i.e. the low frequency part of the Fourier domain splitting. Note that B_0 does not contain a zero of s_α if $\alpha > 0$ but still a (possibly small) local minimum of s_α^2 at $\boldsymbol{\xi} = 0$. Since $B_0 = \emptyset$ for $\alpha \geq \varepsilon$, we may restrict to the case $\alpha < \varepsilon$.

By (34) and the assumption $\varepsilon \leq \pi/6$, we have $|\boldsymbol{\xi}|^2/(2\mathbf{f}) + \alpha \in [0; \pi/6)$ and hence $s_\alpha(\boldsymbol{\xi})^2 \geq C_0(|\boldsymbol{\xi}|^2/(2\mathbf{f}) + \alpha)^2$ for all $\boldsymbol{\xi} \in B_0$ with $C_0 := \sin(\pi/6)^2/(\pi/6)^2$. This implies

$$(36) \quad J_0 = \int_{B_0} s_\alpha(\boldsymbol{\xi})^2 |\hat{\varphi}(\boldsymbol{\xi})|^2 \, d\boldsymbol{\xi} \geq C_0 \int_{B_0} \left(\frac{|\boldsymbol{\xi}|^4}{4\mathbf{f}^2} + \frac{\alpha|\boldsymbol{\xi}|^2}{\mathbf{f}} + \alpha^2 \right) |\hat{\varphi}(\boldsymbol{\xi})|^2 \, d\boldsymbol{\xi}$$

From (36), it can be seen that J_0 is bounded from below by $\alpha^2 \|\hat{\varphi}|_{B_0}\|^2$ and thus indeed stable if $\alpha \neq 0$. However, since α is typically (almost) zero in hard X-ray imaging, we have to resort to the integral summands that involve powers of $|\boldsymbol{\xi}|^2$ in order to achieve robust estimates. These integrands have a zero at $\boldsymbol{\xi} = 0 \in B_0$, which is why smoothness of $|\hat{\varphi}|^2$ has to be exploited to obtain reasonable estimates. This is achieved by the following lemma:

LEMMA 8. Let $D := \{\mathbf{x} \in \mathbb{R}^m : |\mathbf{x}| \leq a\}$ be a closed concentric ball of radius a in \mathbb{R}^m . Let $g, w \in \mathcal{C}^2(D)$ where w is radially symmetric, i.e. $w(\mathbf{x}) = w_0(|\mathbf{x}|)$ for all $\mathbf{x} \in D$ and some function $w_0 : [0; a] \rightarrow \mathbb{R}$. Then

$$\int_D \Delta w \cdot g \, d\mathbf{x} = \frac{mw'_0(a)}{a} \int_D g \, d\mathbf{x} + \int_D \left(\frac{w'_0(a)}{2a} (a^2 - |\mathbf{x}|^2) - (w_0(a) - w) \right) \Delta g \, d\mathbf{x}.$$

Proof. By Green's second identity we have

$$\begin{aligned} (37) \quad \int_D \Delta w \cdot g \, d\mathbf{x} &= \int_D w \cdot \Delta g \, d\mathbf{x} + \int_{\partial D} \left(g \frac{\partial w}{\partial \mathbf{n}} - w \frac{\partial g}{\partial \mathbf{n}} \right) dS(x) \\ &= \int_D w \cdot \Delta g \, d\mathbf{x} + w'_0(a) \int_{\partial D} g \, dS(x) - w_0(a) \int_{\partial D} \frac{\partial g}{\partial \mathbf{n}} dS(x). \end{aligned}$$

Here, $\partial/(\partial \mathbf{n})$ denotes the derivative along the unit normal vector pointing to the outside of ∂D . The boundary terms can be eliminated via the relations

$$\begin{aligned} \int_{\partial D} \frac{\partial g}{\partial \mathbf{n}} dS(x) &= \int_D \Delta g \, d\mathbf{x} \\ \int_{\partial D} g \, dS(x) &= \frac{1}{2a} \int_{\partial D} g \frac{\partial(|\mathbf{x}|^2)}{\partial \mathbf{n}} dS(x) \\ &= \frac{1}{2a} \left(\int_{\partial D} |\mathbf{x}|^2 \frac{\partial g}{\partial \mathbf{n}} dS(x) + 2m \int_D g \, d\mathbf{x} - \int_D |\mathbf{x}|^2 \Delta g \, d\mathbf{x} \right) \\ &= \frac{1}{2a} \left(2m \int_D g \, d\mathbf{x} + \int_D (a^2 - |\mathbf{x}|^2) \Delta g \, d\mathbf{x} \right), \end{aligned}$$

which again follow from Green's second identity. Plugging this into (37) yields the claimed identity. \square

As the functions $\boldsymbol{\xi} \mapsto |\boldsymbol{\xi}|^2$ and $\boldsymbol{\xi} \mapsto |\boldsymbol{\xi}|^4$ are radially symmetric and since B_0 is a concentric ball of radius b_0 , we find that Lemma 8 can be applied to the integrals in (36). This yields the following estimate for the considered low-frequency subdomain:

LEMMA 9. Let $\alpha < \varepsilon \leq \pi/6$ and $B_0^- := \{\boldsymbol{\xi} \in B_0 : \Delta|\hat{\varphi}|^2(\boldsymbol{\xi}) \leq 0\}$. Then

$$\begin{aligned} (38) \quad J_0 &\geq C_0 \left(\left(\frac{m}{m+4} (\varepsilon - \alpha)^2 + \frac{2m}{m+2} \alpha (\varepsilon - \alpha) + \alpha^2 \right) \|\hat{\varphi}|_{B_0}\|^2 \right. \\ &\quad \left. + \int_{B_0^-} \Delta|\hat{\varphi}|^2 \, d\boldsymbol{\xi} \right). \end{aligned}$$

Proof. For the functions $w_1(\boldsymbol{\xi}) := |\boldsymbol{\xi}|^6/(6(m+4))$ and $w_2(\boldsymbol{\xi}) := |\boldsymbol{\xi}|^4/(4(m+2))$, we have that $\Delta w_1(\boldsymbol{\xi}) = |\boldsymbol{\xi}|^4$ and $\Delta w_2(\boldsymbol{\xi}) = |\boldsymbol{\xi}|^2$ for all $\boldsymbol{\xi} \in \mathbb{R}^m$. Accordingly, the integral in (36) matches the setting of Lemma 8. An application gives

$$\begin{aligned} \int_{B_0} |\boldsymbol{\xi}|^4 |\hat{\varphi}(\boldsymbol{\xi})|^2 \, d\boldsymbol{\xi} &= \int_{B_0} \Delta w_1(\boldsymbol{\xi}) |\hat{\varphi}(\boldsymbol{\xi})|^2 \, d\boldsymbol{\xi} \\ &= \frac{mb_0^4}{m+4} \int_{B_0} |\hat{\varphi}(\boldsymbol{\xi})|^2 \, d\boldsymbol{\xi} + \frac{1}{m+4} \int_{B_0} \left(\frac{b_0^4}{2} (b_0^2 - |\boldsymbol{\xi}|^2) - \frac{1}{6} (b_0^6 - |\boldsymbol{\xi}|^6) \right) \Delta |\hat{\varphi}(\boldsymbol{\xi})|^2 \, d\boldsymbol{\xi} \\ &\geq \frac{mb_0^4}{m+4} \int_{B_0} |\hat{\varphi}(\boldsymbol{\xi})|^2 \, d\boldsymbol{\xi} + \frac{b_0^6}{3(m+4)} \int_{B_0^-} \Delta |\hat{\varphi}(\boldsymbol{\xi})|^2 \, d\boldsymbol{\xi} \end{aligned}$$

Here, the integral over $\Delta|\hat{\varphi}|^2$ has been bounded from below by the integral within the sub-domain $B_0^- = \{\mathbf{x} \in B_0 : \Delta|\hat{\varphi}|^2(\mathbf{x}) \leq 0\}$ multiplied by the maximum of the non-negative factor $(b_0^4/2)(b_0^2 - |\boldsymbol{\xi}|^2) - \frac{1}{6}(b_0^6 - |\boldsymbol{\xi}|^6)$. Analogously we obtain

$$\begin{aligned} \int_{B_0} |\boldsymbol{\xi}|^2 |\hat{\varphi}(\boldsymbol{\xi})|^2 \, d\boldsymbol{\xi} &= \int_{B_0} \Delta w_2(\boldsymbol{\xi}) |\hat{\varphi}(\boldsymbol{\xi})|^2 \, d\boldsymbol{\xi} \\ &= \frac{mb_0^2}{m+2} \int_{B_0} |\hat{\varphi}(\boldsymbol{\xi})|^2 \, d\boldsymbol{\xi} + \frac{1}{m+2} \int_{B_0} \left(\frac{b_0^2}{2} (b_0^2 - |\boldsymbol{\xi}|^2) - \frac{1}{4} (b_0^2 - |\boldsymbol{\xi}|^2) \right) \Delta |\hat{\varphi}(\boldsymbol{\xi})|^2 \, d\boldsymbol{\xi} \\ &\geq \frac{mb_0^2}{m+2} \int_{B_0} |\hat{\varphi}(\boldsymbol{\xi})|^2 \, d\boldsymbol{\xi} + \frac{b_0^4}{4(m+2)} \int_{B_0^-} \Delta |\hat{\varphi}(\boldsymbol{\xi})|^2 \, d\boldsymbol{\xi} \end{aligned}$$

Inserting these relations into (36) yields

$$\begin{aligned} J_0 &\geq C_0 \int_{B_0} \left(\frac{|\boldsymbol{\xi}|^4}{4\mathfrak{f}^2} + \frac{\alpha|\boldsymbol{\xi}|^2}{\mathfrak{f}} + \alpha^2 \right) |\hat{\varphi}(\boldsymbol{\xi})|^2 \, d\boldsymbol{\xi} \\ &\geq C_0 \left(\frac{mb_0^4}{4\mathfrak{f}^2(m+4)} + \frac{m\alpha b_0^2}{\mathfrak{f}(m+2)} + \alpha^2 \right) \int_{B_0} |\hat{\varphi}(\boldsymbol{\xi})|^2 \, d\boldsymbol{\xi} \\ &\quad + C_0 \left(\frac{b_0^6}{12\mathfrak{f}^2(m+4)} + \frac{b_0^4\alpha}{4\mathfrak{f}(m+2)} \right) \int_{B_0^-} \Delta |\hat{\varphi}(\boldsymbol{\xi})|^2 \, d\boldsymbol{\xi}. \end{aligned}$$

Re-substituting $b_0 = (2\mathfrak{f})^{\frac{1}{2}}(\epsilon - \alpha)^{\frac{1}{2}}$ into this estimate gives the assertion. \square

4.3. Estimate for the first order CTF-zeros. Before we can derive a global stability estimate from (38), we have to consider the remaining integrals J_j , $j \geq 1$ in the Fourier domain splitting (33). The integration domains B_j are annular shells around the first order zero-manifolds $Z_j = \{\boldsymbol{\xi} \in \mathbb{R}^m : |\boldsymbol{\xi}| = \xi_j\}$, $j \in \mathbb{N}$ of the CTF s_α . According to (34), we have $|\boldsymbol{\xi}|^2/(2\mathfrak{f}) + \alpha - j\pi \in (-\epsilon; \epsilon)$ for all $\boldsymbol{\xi} \in B_j$ and thus

$$(39) \quad s_\alpha(\boldsymbol{\xi})^2 = \sin \left(\frac{|\boldsymbol{\xi}|^2}{2\mathfrak{f}} + \alpha + j\pi \right)^2 \geq \frac{\sin(\epsilon)^2}{\epsilon^2} \left(\frac{|\boldsymbol{\xi}|^2}{2\mathfrak{f}} + \alpha + j\pi \right)^2 \stackrel{\epsilon \leq \frac{\pi}{6}}{\geq} \frac{C_0}{4\mathfrak{f}^2} (|\boldsymbol{\xi}|^2 - \xi_j^2)^2.$$

Using that $(|\boldsymbol{\xi}|^2 - \xi_j^2)^2 = (|\boldsymbol{\xi}| + \xi_j)^2 (|\boldsymbol{\xi}| - \xi_j)^2 \geq (b_{j-} + \xi_j)^2 (|\boldsymbol{\xi}| - \xi_j)^2$, this yields

$$(40) \quad J_j = \int_{B_j} s_\alpha(\boldsymbol{\xi})^2 |\hat{\varphi}(\boldsymbol{\xi})|^2 \, d\boldsymbol{\xi} \geq \frac{C_0(b_{j-} + \xi_j)^2}{4\mathfrak{f}^2} \tilde{J}_j, \quad \tilde{J}_j := \int_{B_j} (|\boldsymbol{\xi}| - \xi_j)^2 |\hat{\varphi}(\boldsymbol{\xi})|^2 \, d\boldsymbol{\xi}.$$

for $j \in \mathbb{N}$. Accordingly, we have to estimate polynomially weighted integrals, similar to the preceding section, yet within the shell-shaped domains B_j instead of a concentric ball. We achieve this by introducing polar coordinates and applying Lemma 8 to the resulting one-dimensional radial integrals:

LEMMA 10 (Stability estimate for the first order CTF-zeros). *Let $0 < \epsilon \leq \pi/6$ and $j \in \mathbb{N}$. Then there exists a measurable subset $B_j^- \subset B_j$ and a constant $0 < C_1 \leq 1/4$, which depends only on m , such that*

$$(41) \quad J_j \geq C_0 \left(C_1 \epsilon^2 \|\hat{\varphi}|_{B_j}\|^2 + \frac{\epsilon^4 \mathfrak{f}}{32(j\pi - \alpha)} \int_{B_j^-} \Delta |\hat{\varphi}|^2(\boldsymbol{\xi}) \, d\boldsymbol{\xi} \right).$$

Proof. Let $j \in \mathbb{N}$ arbitrary. In order to make [Lemma 8](#) applicable to the present setting, we rewrite the integral \tilde{J}_j in [\(40\)](#) by introducing polar coordinates $\boldsymbol{\xi} = \xi \boldsymbol{\theta}$, $\xi \geq 0$, $\boldsymbol{\theta} \in \mathbb{S}^{m-1}$ (\mathbb{S}^{m-1} : unit sphere in \mathbb{R}^m). With the notation in [\(34\)](#), this yields

$$(42) \quad \tilde{J}_j = \int_{b_{j-}}^{b_{j+}} (\xi - \xi_j)^2 \xi^{m-1} \varphi_{\text{rad}}(\xi) \, d\xi, \quad \varphi_{\text{rad}}(\xi) := \int_{\mathbb{S}^{m-1}} |\hat{\varphi}(\xi \boldsymbol{\theta})|^2 \, d\boldsymbol{\theta}.$$

Setting $a_j := b_{j+} - \xi_j$, $\eta := \xi - \xi_j$, $\varphi_j(\xi - \xi_j) := \xi^{(m-1)/2} \varphi_{\text{rad}}(\xi)$, we obtain the bound

$$(43) \quad \begin{aligned} \tilde{J}_j &= \int_{\xi_j - a_j}^{\xi_j + a_j} (\xi - \xi_j)^2 \xi^{\frac{m-1}{2}} \varphi_j(\xi - \xi_j) \, d\xi + \int_{b_{j-}}^{\xi_j - a_j} (\xi - \xi_j)^2 \xi^{m-1} \varphi_{\text{rad}}(\xi) \, d\xi \\ &\geq (\xi_j - a_j)^{\frac{m-1}{2}} \int_{-a_j}^{a_j} \eta^2 \varphi_j(\eta) \, d\eta + a_j^2 \int_{b_{j-}}^{\xi_j - a_j} \xi^{m-1} \varphi_{\text{rad}}(\xi) \, d\xi. \end{aligned}$$

The first integral on the right hand side of [\(43\)](#) matches the setting of [Lemma 8](#) in $m = 1$ dimensions with weight function $w(\eta) := \eta^4/12$. This yields

$$(44) \quad \begin{aligned} \int_{-a_j}^{a_j} \eta^2 \varphi_j(\eta) \, d\eta &= \frac{a_j^2}{3} \int_{-a_j}^{a_j} \varphi_j(\eta) \, d\eta + \int_{-a_j}^{a_j} \left(\frac{a_j^2(a_j^2 - \eta^2)}{6} - \frac{a_j^4 - \eta^4}{12} \right) \varphi_j''(\eta) \, d\eta \\ &\geq \frac{a_j^2}{3} \int_{-a_j}^{a_j} \varphi_j(\eta) \, d\eta + \frac{a_j^4}{12} \int_{I_j^-} \varphi_j''(\eta) \, d\eta, \end{aligned}$$

where we have set $I_j^- := \{\eta \in [-a_j; a_j] : \varphi_j''(\eta) \leq 0\}$ and used that $0 \leq (a_j^2/6)(a_j^2 - \eta^2) - (a_j^4 - \eta^4)/12 \leq a_j^4/12$. Setting $B_j^- := \{\boldsymbol{\xi} \in B_j : |\boldsymbol{\xi}| \in I_j^- + \xi_j\}$ and re-substituting φ_{rad} and $|\hat{\varphi}|^2$ for φ_j , we estimate the second integral in [\(44\)](#) by

$$(45) \quad \begin{aligned} &\underbrace{(\xi_j - a_j)^{\frac{m-1}{2}}}_{\leq \xi^{(m-1)/2} \text{ for } \xi \in I_j^- + \xi_j} \int_{I_j^-} \underbrace{\varphi_j''(\eta)}_{\leq 0} \, d\eta \geq \int_{I_j^- + \xi_j} \xi^{\frac{m-1}{2}} \partial_\xi^2 \left(\xi^{\frac{m-1}{2}} \varphi_{\text{rad}}(\xi) \right) \, d\xi \\ &= \int_{I_j^- + \xi_j} \xi^{m-1} \int_{\mathbb{S}^{m-1}} \left(\partial_\xi^2 + \frac{m-1}{\xi} \partial_\xi + \frac{(m-1)(m-3)}{4\xi^2} \right) |\hat{\varphi}(\xi \boldsymbol{\theta})|^2 \, d\boldsymbol{\theta} \, d\xi \\ &= \int_{B_j^-} \left(\Delta + \frac{(m-1)(m-3)}{4|\boldsymbol{\xi}|^2} \right) |\hat{\varphi}|^2(\xi \boldsymbol{\theta}) \, d\boldsymbol{\xi} \\ &\geq \int_{B_j^-} \Delta |\hat{\varphi}|^2(\boldsymbol{\xi}) \, d\boldsymbol{\xi} - \frac{\delta_{m2}}{4b_{j-}^2} \int_{B_j^-} |\hat{\varphi}|^2(\boldsymbol{\xi}) \, d\boldsymbol{\xi}. \end{aligned}$$

Here we have identified the radial part of the Laplacian in polar coordinates and implicitly added the angular part, which does not contribute to the \mathbb{S}^{m-1} -integrals. The inequality in the last line follows from the fact that $(m-1)(m-3)/(4|\boldsymbol{\xi}|^2)$ is negative only for $m = 2$, in which case it is bounded by the given term (δ_{ij} : Kronecker-Delta). Re-substituting $|\hat{\varphi}|^2$ in the remaining integrals in [\(43\)](#) and [\(44\)](#) gives

$$(46) \quad \begin{aligned} &(\xi_j - a_j)^{\frac{m-1}{2}} \frac{a_j^2}{3} \int_{-a_j}^{a_j} \varphi_j(\eta) \, d\eta + a_j^2 \int_{b_{j-}}^{\xi_j - a_j} \xi^{m-1} \varphi_{\text{rad}}(\xi) \, d\xi \\ &\geq \left(\frac{\xi_j - a_j}{\xi_j + a_j} \right)^{\frac{m-1}{2}} \frac{a_j^2}{3} \int_{\xi_j - a_j}^{\xi_j + a_j} \xi^{m-1} \varphi_{\text{rad}}(\xi) \, d\xi + a_j^2 \int_{b_{j-}}^{\xi_j - a_j} \xi^{m-1} \varphi_{\text{rad}}(\xi) \, d\xi \\ &\geq \left(\frac{\xi_j - a_j}{\xi_j + a_j} \right)^{\frac{m-1}{2}} \frac{a_j^2}{3} \int_{b_{j-}}^{b_{j+}} \xi^{m-1} \int_{\mathbb{S}^{m-1}} |\hat{\varphi}|^2(\xi \boldsymbol{\theta}) \, d\boldsymbol{\theta} \, d\xi = \left(\frac{\xi_j - a_j}{\xi_j + a_j} \right)^{\frac{m-1}{2}} \frac{a_j^2}{3} \|\hat{\varphi}|_{B_j}\|^2. \end{aligned}$$

Combining the estimates (43), (44), (45) and (46), we thus obtain for all $j \in \mathbb{N}$

$$(47) \quad \tilde{J}_j \geq \underbrace{\frac{a_j^2}{3} \left(\left(\frac{\xi_j - a_j}{\xi_j + a_j} \right)^{\frac{m-1}{2}} - \frac{a_j^2}{16b_{j-}^2} \right)}_{=:\lambda} \|\hat{\varphi}|_{B_j}\|^2 + \underbrace{\frac{a_j^4}{12}}_{=:\mu} \int_{B_j^-} \Delta |\hat{\varphi}|^2(\xi) \, d\xi$$

What remains to be done is to derive uniform bounds for the constants in (47) within the assumed parameter range $j \in \mathbb{N}$, $\alpha \leq \pi/2$ and $0 < \varepsilon \leq \pi/6$. First, we have $\xi_j^2 = 2\mathfrak{f}(\pi j - \alpha) \geq \pi\mathfrak{f}$ and hence by Taylor-expansion of the square-root

$$(48) \quad a_j = (\xi_j^2 + 2\mathfrak{f}\varepsilon)^{\frac{1}{2}} - \xi_j \in \frac{\varepsilon\mathfrak{f}}{\xi_j} \cdot \left[1 - \frac{\varepsilon\mathfrak{f}}{2\xi_j^2}; 1 \right] \subset \frac{\varepsilon\mathfrak{f}}{\xi_j} \cdot \left[1 - \frac{\varepsilon}{2\pi}; 1 \right] \subset \frac{\varepsilon\mathfrak{f}}{\xi_j} \cdot \left[\frac{11}{12}; 1 \right].$$

Using (48) along with $b_{j-}^2 = \xi_j^2 - 2\mathfrak{f}\varepsilon \stackrel{\varepsilon \leq \pi/6}{\geq} \xi_j^2 - \pi\mathfrak{f}/3 \stackrel{\xi_j^2 \geq \pi\mathfrak{f}}{\geq} 2\pi\mathfrak{f}/3$ furthermore gives

$$(49a) \quad \frac{a_j^2}{16b_{j-}^2} \stackrel{(48)}{\leq} \frac{\varepsilon^2\mathfrak{f}^2}{16\xi_j^2(\xi_j^2 - 2\mathfrak{f}\varepsilon)} \leq \frac{3\varepsilon^2}{32\pi^2} \leq \frac{1}{384}$$

$$(49b) \quad \left(\frac{\xi_j - a_j}{\xi_j + a_j} \right)^{\frac{1}{2}} \geq 1 - \frac{a_j}{\xi_j} \stackrel{(48)}{\geq} 1 - \frac{\varepsilon\mathfrak{f}}{\xi_j^2} \geq 1 - \frac{\varepsilon}{\pi} \geq \frac{5}{6}$$

Combining (48) and (49) gives $\lambda \geq (4/3)C_1\varepsilon^2\mathfrak{f}^2/\xi_j^2$ with $C_1 := (121/576)((5/6)^{m-1} - \delta_{m2}/384)$ and $\mu \leq \varepsilon^4\mathfrak{f}^4/(12\xi_j^4)$. Substituting these bounds into (47), we obtain

$$(50) \quad \tilde{J}_j \geq \frac{4\mathfrak{f}^2}{3\xi_j^2} \left(C_1 \|\hat{\varphi}|_{B_j}\|^2 + \frac{\varepsilon^4\mathfrak{f}^2}{16\xi_j^2} \int_{B_j^-} \Delta |\hat{\varphi}|^2(\xi) \, d\xi \right).$$

Now the assertion follows by inserting (47) into (40), using that $\mathfrak{f}/\xi_j^2 = 1/(2(j\pi - \alpha))$ and $(\xi_j + b_{j-})^2 > 3\xi_j^2$ according to the estimate $b_{j-}^2 \geq 2\xi_j^2/3$. \square

4.4. Global stability results. With the bounds for different subdomains of the Fourier space obtained in Lemmas 9 and 10, we are now in a position to prove a global stability result for Inverse Problem 2. For $\varepsilon > \alpha$, an application of the estimates (35), (38) and (41) to the sub-integrals in (33) and Lemma 7 with $\Omega = \overline{B(0, 1/2)}$ yields

$$(51) \quad \begin{aligned} \|s_\alpha \cdot \hat{\varphi}\|^2 &\geq C_0 \left(\zeta(\varepsilon, \alpha) \|\varphi\|^2 + \mathfrak{f}\eta(\varepsilon, \alpha) \int_{B^-} \Delta |\hat{\varphi}|^2 \, d\xi \right) \\ &\geq C_0 \left(\zeta(\varepsilon, \alpha) - \frac{\mathfrak{f}}{2}\eta(\varepsilon, \alpha) \right) \|\varphi\|^2 \end{aligned}$$

Here, we have used that $\|\hat{\varphi}|_{D_\varepsilon}\|^2 + \sum_{j=0}^{\infty} \|\hat{\varphi}|_{B_j}\|^2 = \|\hat{\varphi}\|^2 = \|\varphi\|$ by the disjoint Fourier domain splitting in §4.1 and defined $B^- := \bigcup_{j=0}^{\infty} B_j^-$ as well as

$$(52a) \quad \begin{aligned} \zeta(\varepsilon, \alpha) &:= \min \left\{ \frac{m}{m+4}(\varepsilon - \alpha)^2 + \frac{2m}{m+2}\alpha(\varepsilon - \alpha) + \alpha^2, C_1\varepsilon^2 \right\}, \\ \eta(\varepsilon, \alpha) &:= \max \left\{ \frac{2}{3(m+4)}(\varepsilon - \alpha)^3 + \frac{1}{m+2}\alpha(\varepsilon - \alpha)^2, \frac{1}{32(\pi - \alpha)}\varepsilon^4 \right\} \end{aligned} \quad \text{for } \varepsilon > \alpha.$$

Note that the bounding constant $\sin(\varepsilon)$ for the integral J_ε does not appear in $\zeta(\varepsilon, \alpha)$ as $\sin(\varepsilon) \geq C_1\varepsilon^2$ holds true within the entire parameter range $0 \leq \varepsilon \leq \pi/6$.

In the case $\varepsilon \leq \alpha$, the subdomains $B_0^- \subset B_0 = \emptyset$ are empty so that contributions from the sub-integral J_0 can be suppressed in the estimate (51). Hence, we may set

$$(52b) \quad \zeta(\varepsilon, \alpha) := C_1 \varepsilon^2, \quad \eta(\varepsilon, \alpha) := \frac{\varepsilon^4}{32(\pi - \alpha)} \quad \text{for } \varepsilon \leq \alpha.$$

Since $\eta(\varepsilon, \alpha)$ is of higher-order in ε than $\zeta(\varepsilon, \alpha)$ according to (52a) and (52b), it is possible to find an optimal value $\varepsilon = \varepsilon_{\text{opt}}(\alpha, \mathbf{f})$ such that the constant on the right-hand side of (51) is maximal and in particular positive. This idea leads to the sought estimates for the stability constant $C_{\text{IP}2}(\Omega, \mathbf{f}, \alpha)$ in [Theorem 2](#):

Proof of [Theorem 2](#). We first study the regime $\varepsilon \geq \alpha$, as is necessary in particular if $\alpha = 0$. Since

$$\begin{aligned} & \frac{m}{m+4}(\varepsilon - \alpha)^2 + \frac{2m}{m+2}\alpha(\varepsilon - \alpha) + \alpha^2 \\ &= \frac{m}{m+4}\varepsilon^2 + \left(\frac{2m}{m+2} - \frac{2m}{m+4}\right)\alpha(\varepsilon - \alpha) + \left(\frac{m}{m+4} - \frac{2m}{m+2} + 1\right)\alpha^2 \geq \frac{m}{m+4}\varepsilon^2, \end{aligned}$$

(52a) yields the bound

$$(53) \quad \zeta(\varepsilon, \alpha) \geq \zeta_0 \varepsilon^2, \quad \zeta_0 := \min\left\{C_1, \frac{m}{m+4}\right\}.$$

To bound η in (52a) we observe that $\alpha(\varepsilon - \alpha)^2 \leq 4\varepsilon^3/27$ for $0 \leq \alpha < \varepsilon$ to obtain

$$\frac{2}{3(m+4)}(\varepsilon - \alpha)^3 + \frac{1}{m+2}\alpha(\varepsilon - \alpha)^2 \leq \left(\frac{2}{3(m+4)} + \frac{4}{27(m+2)}\right)\varepsilon^3 \leq \left(\frac{2}{15} + \frac{4}{81}\right)\varepsilon^3 < \frac{1}{5}\varepsilon^3.$$

As $\frac{\varepsilon}{32(\pi - \alpha)} < \frac{1}{5}$ for $0 \leq \alpha \leq \varepsilon \leq \frac{\pi}{6}$ this implies by (52a)

$$(54) \quad \eta(\varepsilon, \alpha) \leq \frac{1}{5}\varepsilon^3.$$

A comparison with (52b) shows that the estimates (53) and (54) remain valid for $\varepsilon < \alpha$ and thus hold for all $0 \leq \varepsilon \leq \pi/6$.

Now we apply the derived bounds on $\zeta(\varepsilon, \alpha)$ and $\eta(\varepsilon, \alpha)$ in (51) to estimate the stability constant of [Inverse Problem 2](#):

$$(55) \quad \begin{aligned} C_{\text{IP}2}(\Omega, \mathbf{f}, \alpha)^2 &= \inf_{\varphi \in L^2_{\Omega}, \|\varphi\|=1} \|S\varphi\|^2 \stackrel{(31)}{=} \inf_{\varphi \in L^2_{\Omega}, \|\varphi\|=1} 4 \|s_{\alpha} \cdot \hat{\varphi}\|^2 \\ &\geq \sup_{0 \leq \varepsilon \leq \pi/6} 4C_0\varepsilon^2 \left(\zeta_0 - \frac{1}{10}\mathbf{f}\varepsilon\right) = \begin{cases} \frac{1600C_0\zeta_0^3}{27\mathbf{f}^2} & \text{if } \mathbf{f} \geq \frac{40\zeta_0}{\pi} \\ \frac{\pi^2 C_0}{9} \left(\zeta_0 - \frac{\pi}{60}\mathbf{f}\right) & \text{if } \mathbf{f} < \frac{40\zeta_0}{\pi} \end{cases} \\ &\geq \min\{c_1^2, c_2^2 \mathbf{f}^{-2}\} \end{aligned}$$

The supremum is attained at $\varepsilon = \varepsilon_{\text{opt}} := \min\{\pi/6, 20\zeta_0/(3\mathbf{f})\}$, and we have defined $c_1 := (\pi^2 C_0 \zeta_0 / 27)^{1/2}$ and $c_2 := (1600 C_0 \zeta_0^3 / 27)^{1/2}$.

It remains to show improved bounds for $\alpha > 0$ and large \mathbf{f} . Here we choose $0 \leq \varepsilon \leq \alpha/3$ to satisfy $\varepsilon \leq \pi/6$ for all $\alpha \in (0, \pi/2]$. Moreover, we make use of the simplified expressions for ζ and η in (52b), that apply in this parameter range. Inserting (52b) into (51) and using that $\pi - \alpha \geq \pi/2$ gives

$$(56) \quad \begin{aligned} 4 \|s_{\alpha} \cdot \hat{\varphi}\|^2 &\geq \sup_{0 < \varepsilon \leq \alpha/3} 4C_0\varepsilon^2 \left(C_1 - \frac{1}{64(\pi - \alpha)}\mathbf{f}\varepsilon^2\right) \geq \sup_{0 < \varepsilon \leq \alpha/3} 4C_0\varepsilon^2 \left(C_1 - \frac{1}{32\pi}\mathbf{f}\varepsilon^2\right) \\ &= \begin{cases} \frac{32\pi C_0 C_1^2}{\mathbf{f}} & \text{if } \mathbf{f} \geq \frac{144\pi C_1}{\alpha^2} \\ \frac{4C_0\alpha^2}{9} \left(C_1 - \frac{\alpha^2 \mathbf{f}}{288\pi}\right) & \text{if } \mathbf{f} < \frac{144\pi C_1}{\alpha^2} \end{cases} \\ &\geq \min\{c_3^2 \alpha^2, c_4^2 \mathbf{f}^{-1}\} \end{aligned}$$

for all $\varphi \in L^2_\Omega$ with $\|\varphi\| = 1$. Here, the constants are chosen as $c_3 := (2C_0C_1/9)^{1/2}$ and $c_4 := (32\pi C_0)^{1/2}C_1$ and the supremum is attained at $\varepsilon_{\text{opt}} = \min\{\alpha/3, (16\pi C_1/\mathfrak{f})^{1/2}\}$. Combining (55) and (56) yields the claimed stability estimate (12). \square

4.5. Optimality. As opposed to the analysis of [Inverse Problem 1](#), the bounds on the stability constant C_{IP2} derived in this section can be expected to be highly non-optimal: the principal derivative-bound (32) is clearly not sharp and various additional estimates have been made in [Lemma 9](#), [Lemma 10](#) and in the proof of [Theorem 2](#) just to simplify the arising terms. Accordingly, the obtained numerical values for the constants c_j in (12) can be expected to be *overly pessimistic*. Sharper characterizations may be achieved by numerically computing the minimal singular value of the forward operator S by a similar approach as in §3.5.

Independently of such numerical refinements, it is of interest whether the achieved analytical bounds $C_{\text{IP2}}(\Omega, \mathfrak{f}, \alpha) \gtrsim \mathfrak{f}^{-\nu}$ are at least of *optimal order* ν in the Fresnel number \mathfrak{f} for $\mathfrak{f} \rightarrow \infty$. A positive answer is given by the following theorem:

THEOREM 11 (Order-optimality of the stability bounds for [Inverse Problem 2](#)).
Within the setting of [Theorem 2](#), let $c'_1, c'_2, \nu > 0$ be constants such that

$$(57) \quad C_{\text{IP2}}(\Omega, \mathfrak{f}, 0) \geq \min\{c'_1, c'_2 \mathfrak{f}^{-\nu}\} \quad \text{for all } \mathfrak{f} > 0.$$

Then $\nu \geq 1$, i.e. the bound (12) is of optimal asymptotic order in \mathfrak{f} for $\alpha = 0$.

Proof. Assume $\nu < 1$. Let $\alpha = 0$ and $\varphi \in L^2_\Omega \cap \mathcal{C}^2(\mathbb{R}^m)$ with $\|\varphi\| = 1$. Then we have by the definition of the forward operator in (9)

$$(58) \quad \begin{aligned} \|S_0\varphi\| &= 2 \|s_\alpha \cdot \mathcal{F}(\varphi)\| = 2 \left(\int_{\mathbb{R}^m} \sin\left(\frac{|\xi|^2}{2\mathfrak{f}}\right)^2 |\mathcal{F}(\varphi)(\xi)|^2 d\xi \right)^{1/2} \\ &\leq \frac{\sin(x)^2 \leq x^2}{\mathfrak{f}} \frac{1}{\mathfrak{f}} \left(\int_{\mathbb{R}^m} |\xi|^2 |\mathcal{F}(\varphi)(\xi)|^2 d\xi \right)^{1/2} = \mathfrak{f}^{-1} \|\Delta\varphi\|. \end{aligned}$$

Note that $\|\Delta\varphi\| \neq 0$ by the maximum principle since Ω is bounded. Now let $\mathfrak{f} > \max\{(c'_1/c'_2)^{-1/\nu}, (2\pi c'_2/\|\Delta\varphi\|)^{1/(1-\nu)}\}$. Then (57) and (58) imply

$$C_{\text{IP2}}(\Omega, \mathfrak{f}, 0) \stackrel{c'_2 \mathfrak{f}^{-\nu} < c'_1}{=} c'_2 \mathfrak{f}^{-\nu} = \frac{2\pi c'_2 \mathfrak{f}^{1-\nu}}{\|\Delta\varphi\|} \mathfrak{f}^{-1} \|\Delta\varphi\| \stackrel{(58)}{\geq} \frac{2\pi c'_2 \mathfrak{f}^{1-\nu}}{\|\Delta\varphi\|} \|S_0\varphi\| > \|S_0\varphi\|.$$

Since $\|\varphi\| = 1$, this contradicts the definition of the stability constant C_{IP2} . Hence, $\nu \geq 1$ must hold by contradiction. \square

Intuitively, the upper bound $-\nu \leq -1$ for the achievable order in [Theorem 11](#) is related to the *second* order zero of the CTF s_α at $\xi = 0$ for $\alpha = 0$, which allows to bound $|s_\alpha|$ by a quadratic function. In the case $\alpha > 0$, this zero no longer exists which enables higher order behavior $C_{\text{IP2}} \gtrsim \mathfrak{f}^{-1/2}$ as shown in [Theorem 2](#). As the CTF still has *first order* zero manifolds, we conjecture that this rate is likewise of optimal order. However, simple arguments as in the proof of [Theorem 11](#) suffer from technical difficulties arising from the spherical geometry and the \mathfrak{f} -dependence of the first order zero-manifolds. A treatment of the case $\alpha > 0$ is therefore omitted here.

5. Image reconstruction from two measurements. By axial translation of the object in [Figure 1\(a\)](#), holograms I_1, I_2 may be recorded for different sample-detector distances and thus at different Fresnel numbers $f_1 \neq f_2$. It is often stated [[5, 7, 17, 20](#)] that the acquired additional data permits a more stable phase retrieval in this setting - in particular if phase shifts ϕ and attenuation μ are to be recovered as independent parameters. Within the weak object approximation (see [§2.2](#)), this setting amounts to reconstructing $h = -\mu - i\phi$ from measurements $(T_1 h, T_2 h)$, where T_j denotes the linearized forward operator in [\(5\)](#) to the Fresnel number $f = f_j$. Adopting the CTF-formulation in [\(6\)](#), the two-hologram setting is modeled by the forward map

$$(59) \quad S^{(2)} : L^2(\mathbb{R}^m)^2 \rightarrow L^2(\mathbb{R}^m)^2, \quad \mathbf{S}(\boldsymbol{\xi}) := \begin{pmatrix} \sin\left(\frac{|\boldsymbol{\xi}|^2}{2f_1}\right) & -\cos\left(\frac{|\boldsymbol{\xi}|^2}{2f_1}\right) \\ \sin\left(\frac{|\boldsymbol{\xi}|^2}{2f_2}\right) & -\cos\left(\frac{|\boldsymbol{\xi}|^2}{2f_2}\right) \end{pmatrix} \\ \begin{pmatrix} \phi \\ \mu \end{pmatrix} \mapsto 2\mathcal{F}^{-1}(\mathbf{S} \cdot \mathcal{F} \begin{pmatrix} \phi \\ \mu \end{pmatrix}),$$

Here, the matrix-vector-product is to be understood as a point-wise product of the vector- and matrix-valued function values and the (inverse) Fourier transforms $\mathcal{F}, \mathcal{F}^{-1}$ are meant component-wise. Furthermore, we denote by $\|f\| := (\|f_1\|^2 + \|f_2\|^2)^{1/2}$ for $f = (f_1, f_2) \in L^2(\mathbb{R}^m)^2$ the usual norm on $L^2(\mathbb{R}^m)^2$. With the forward model defined in [\(59\)](#), image recovery from two diffraction patterns may then be stated as:

INVERSE PROBLEM 3 (Phase contrast imaging from two measurements). *For given support $\Omega \subset \mathbb{R}^m$, recover the images $\phi, \mu \in L^2_\Omega$ from two noisy holograms*

$$\begin{pmatrix} I_1^\epsilon - 1 \\ I_2^\epsilon - 1 \end{pmatrix} = S^{(2)} \begin{pmatrix} \phi \\ \mu \end{pmatrix} + \boldsymbol{\epsilon} \quad \text{with} \quad \|\boldsymbol{\epsilon}\| \leq \epsilon.$$

As the same amount of object information is to be recovered from a larger data set, it is evident that [Inverse Problem 3](#) cannot be more ill-posed or ill-conditioned than [Inverse Problem 1](#). In order to gain deeper insight, it is illustrative to write down an explicit inverse of the forward operator $S^{(2)}$ defined in [\(59\)](#) by point-wise inversion of the contrast-transfer-matrix \mathbf{S} as done in [[13](#)]: setting $f_- := (f_1^{-1} - f_2^{-1})^{-1}$ this yields for any $(\phi, \mu) \in L^2(\mathbb{R}^m)$

$$(60) \quad \begin{pmatrix} \phi \\ \mu \end{pmatrix} = \mathcal{F}^{-1} \left(\frac{1}{2 \sin\left(\frac{|\boldsymbol{\xi}|^2}{2f_-}\right)} \begin{pmatrix} \cos\left(\frac{|\boldsymbol{\xi}|^2}{2f_2}\right) & -\cos\left(\frac{|\boldsymbol{\xi}|^2}{2f_1}\right) \\ \sin\left(\frac{|\boldsymbol{\xi}|^2}{2f_2}\right) & -\sin\left(\frac{|\boldsymbol{\xi}|^2}{2f_1}\right) \end{pmatrix} \mathcal{F} S^{(2)} \begin{pmatrix} \phi \\ \mu \end{pmatrix} \right).$$

All of the operations on the right-hand side of in [\(60\)](#) are bounded except for the point-wise division by the factor $2 \sin(|\boldsymbol{\xi}|^2/(2f_-))$. According to [\(9\)](#), we find that the latter operation exactly corresponds to solving [Inverse Problem 2](#) for a pure phase object (i.e. $\alpha = 0$) at an effective Fresnel number of $f = f_-$. In particular, this implies that the solution of [Inverse Problem 3](#) is unique but ill-posed without a support constraint, i.e. for general $\phi, \mu \in L^2(\mathbb{R}^m)$. By a more rigorous analysis of the analogy to [Inverse Problem 2](#), we obtain stability estimates:

THEOREM 12 (Stability estimate for [Inverse Problem 3](#)). *Let S_0 denote the forward operator of [Inverse Problem 2](#) for $\alpha = 0$ and $f = f_- := (f_1^{-1} - f_2^{-1})^{-1}$. Then*

$$(61) \quad \|S^{(2)} \begin{pmatrix} \phi \\ \mu \end{pmatrix}\| \geq 2^{-\frac{1}{2}} \|S_0(\phi + i\mu)\| \quad \text{for all real-valued } \phi, \mu \in L^2(\mathbb{R}^m)$$

In particular, for any support-domain $\Omega \subset \mathbb{R}^m$, we have the relative stability estimate

$$(62) \quad \|S^{(2)} \begin{pmatrix} \phi \\ \mu \end{pmatrix}\| \geq 2^{-\frac{1}{2}} C_{\text{IP2}}(\Omega, f_-, 0) \left\| \begin{pmatrix} \phi \\ \mu \end{pmatrix} \right\| \quad \text{for all real-valued } \phi, \mu \in L^2_\Omega.$$

Proof. Let $\phi, \mu \in L^2(\mathbb{R}^m)$ be real-valued. Setting $\hat{\mathbf{h}} := (\mathcal{F}(\phi), \mathcal{F}(\mu))$ and exploiting that \mathcal{F} is unitary, we obtain by (59)

$$\|S^{(2)} \begin{pmatrix} \phi \\ \mu \end{pmatrix}\|^2 = 4\|\mathbf{S}\hat{\mathbf{h}}\|^2 = 4 \int_{\mathbb{R}^m} |\mathbf{S}(\boldsymbol{\xi})\hat{\mathbf{h}}(\boldsymbol{\xi})|^2 d\boldsymbol{\xi}.$$

The integrand $|\mathbf{S}(\boldsymbol{\xi})\hat{\mathbf{h}}(\boldsymbol{\xi})|^2$ is bounded from below by $\sigma_0^2(\boldsymbol{\xi})|\hat{\mathbf{h}}(\boldsymbol{\xi})|^2$ with the smallest singular value $\sigma_0(\boldsymbol{\xi})$ of the 2-by-2 matrix $\mathbf{S}(\boldsymbol{\xi})$. Direct computation shows

$$\sigma_0^2(\boldsymbol{\xi}) = 1 - \left| \cos\left(\frac{|\boldsymbol{\xi}|^2}{2\mathfrak{f}_-}\right) \right| \geq \frac{1}{2} \sin\left(\frac{|\boldsymbol{\xi}|^2}{2\mathfrak{f}_-}\right)^2 \quad \text{for all } \boldsymbol{\xi} \in \mathbb{R}^m.$$

By inserting this result into the previous equation and comparing to (9), we obtain

$$\begin{aligned} \|S^{(2)} \begin{pmatrix} \phi \\ \mu \end{pmatrix}\|^2 &\geq 2 \int_{\mathbb{R}^m} \sin\left(\frac{|\boldsymbol{\xi}|^2}{2\mathfrak{f}_-}\right)^2 |\hat{\mathbf{h}}(\boldsymbol{\xi})|^2 d\boldsymbol{\xi} \\ &= 2 \int_{\mathbb{R}^m} \sin\left(\frac{|\boldsymbol{\xi}|^2}{2\mathfrak{f}_-}\right)^2 |\mathcal{F}(\phi)(\boldsymbol{\xi}) + i\mathcal{F}(\mu)(\boldsymbol{\xi})|^2 d\boldsymbol{\xi} = \frac{1}{2} \|S_0(\phi + i\mu)\|^2. \end{aligned}$$

This proves (61). The second inequality (62) follows by bounding the right-hand side of (61) with the stability constant of [Inverse Problem 2](#). \square

We emphasize that [Theorem 12](#) does not only relate the worst case stability of [Inverse Problems 2](#) and [3](#) but (61) identifies the contrast attained by individual modes under the forward operators S_0 and $S^{(2)}$. Specifically, whenever $\|S_0(\phi + i\mu)\|$ is large, the mode $(\phi, \mu)^\top$ also attains high contrast under the forward map $S^{(2)}$ of [Inverse Problem 3](#). It should furthermore be noted that the derived stability estimates are in terms of the *difference Fresnel number* $\mathfrak{f}_-^{-1} = \mathfrak{f}_1^{-1} - \mathfrak{f}_2^{-1}$. Hence, if the two holograms are recorded at similar Fresnel numbers $\mathfrak{f}_1 \approx \mathfrak{f}_2$, i.e. for only slightly varied setup parameters, \mathfrak{f}_- is very large so that the stability bounds in [Theorem 12](#) will hardly be better than for the *single* measurement case. This is quite intuitive as the second measurement provides only little additional information in such a setting.

6. Discussion and conclusions. In this paper we have studied the stability of phase retrieval in propagation-based phase contrast imaging within the linear contrast-transfer-function model (CTF) [12, 42], valid for weakly interacting objects. While the image reconstruction problem is generally ill-posed and even severely non-unique if both phase-shifts ϕ and attenuation μ are to be recovered from a single (phaseless) intensity measurement ([Inverse Problem 1](#)), we could show *well-posedness* under a support constraint: if the image $h = -\mu - i\phi$ is known to be supported in a bounded domain $\Omega \subset \mathbb{R}^m$, then the attained contrast $\|Th\| \geq C_{\text{IP1}}(\Omega, \mathfrak{f}) \|h\|$ is bounded from below by a positive stability constant $C_{\text{IP1}}(\Omega, \mathfrak{f}) > 0$ according to [Theorem 1](#).

Numerical simulations (see §3.5) suggest that the proven lower bound $C_{\text{IP1}}(\Omega, \mathfrak{f}) \gtrsim \mathfrak{f}^{1/4} \exp(-\mathfrak{f}/8)$ is quite sharp. Accordingly, C_{IP1} unfortunately decays nearly exponentially with the Fresnel number \mathfrak{f} of the imaging setup (computed w.r.t. the support diameter!), which translates into partly ridiculously small values within the typical range $10 \leq \mathfrak{f} \leq 10^3$ in X-ray phase contrast experiments. For instance, the estimate (11) gives $C_{\text{IP1}}(\Omega, 2\pi \cdot 100) \leq 10^{-33}$ at a Fresnel number $\mathfrak{f} = 100$. In other words: although well-posed, the inversion of the forward operator T is typically *heavily ill-conditioned*, admitting amplification of data errors by bounded, yet *huge* factors C_{IP1}^{-1} in the image reconstruction. It is thus not surprising that the independent recovery

of both ϕ and μ from a single hologram is typically severely corrupted by artifacts in practice, see e.g. [24, 37], and commonly considered as not feasible [5, 17, 30].

On the other hand, such a reconstruction has been successfully demonstrated in [26] up to slight low-frequency artifacts. In view of the present work, the key ingredient to this demonstration can be identified as the comparably small Fresnel number $\mathfrak{f} \approx 14$ of the support in the considered setup. By the characterization of the least stable modes in [Theorem 5](#), this corresponds to a minimum contrast

$$(63) \quad \|T\phi_{(0,0)}\| \geq 10^{-4} \|\phi_{(0,0)}\| \quad \text{and} \quad \|T\phi_{(0,1)}\| \geq 7 \cdot 10^{-4} \|\phi_{(0,1)}\|$$

for the least and second least stable image modes $\phi_{(0,0)}$ and $\phi_{(0,1)}$. The reconstruction of these low-frequency image components is thus feasible in principle, yet numerically cumbersome, which explains the residual artifacts in the reconstruction. Higher-order image modes attain contrast in the order of the data noise level or above and may thus be recovered with reasonable accuracy. Our stability estimates thus predict that the joint recovery of phase shifts ϕ and absorption μ is feasible if and only if $\mathfrak{f} \lesssim 10$, i.e. in the *deeply holographic regime* - in excellent agreement with numerical reconstructions.

According to the improved stability estimate for the settings of [Inverse Problems 2](#) and [3](#) (see [Theorems 2](#) and [12](#)) image recovery can be performed without additional regularization provided a sufficiently strong support constraint. This is consistent with the observed high performance of iterative projection algorithms in phase retrieval (see [4, 9, 23] and references therein, mostly for the far-field case and e.g. [3, 11] for near-field phase contrast), which make use of support constraints.

Let us discuss some possible extensions of our results. First of all we have assumed that diffraction patterns can be measured in a whole detector plane, whereas real-world X-ray detectors necessarily cover only a finite area. If intensities are measured only in a bounded subdomain, the singular values of the forward operator T will eventually decay exponentially since T can be written as an integral operator with an analytic (though highly oscillatory) kernel. On the other hand, Fresnel propagation is mathematically equivalent to time-evolution within the free Schrödinger equation (if the z -coordinate in [Fig. 1\(b\)](#) is identified with time). Localization properties of the latter model suggest that the finiteness of the detection domain has little influence if it is chosen sufficiently large - in agreement with experimental and numerical experience. A better understanding and analysis of the impact of a finite field of view will be an interesting goal for future research. Further possible extensions include a treatment of the nonlinear imaging model [\(4\)](#), non-plane wave illumination and partial coherence. Moreover, in *region-of-interest* imaging of extended objects, support constraints do not hold true so that stability needs to be established by other means.

Finally, we emphasize that - although seemingly specific to the considered imaging setup - our analysis treats a fairly general physical problem: the reconstruction of a (compactly supported) perturbation to a plane wave from intensities of the propagated field under the paraxial Helmholtz equation or - equivalently - within time-dependent Schrödinger dynamics. The results may thus be relevant for several related wave-optical and quantum-mechanical inverse problems.

Acknowledgements. We thank Tim Salditt, Aike Ruhlandt and Martin Krenkel from the Institute for X-ray Physics at the University of Göttingen for enlightening discussions on phase contrast setups, a priori constraints and stability of image reconstruction, as well as for providing the experimental data used in [Figures 1](#) and [2](#) for visualization of the theory in this work.

REFERENCES

- [1] HABIB AMMARI, YAT TIN CHOW, AND JUN ZOU, *Phased and phaseless domain reconstructions in the inverse scattering problem via scattering coefficients*, SIAM J. Appl. Math., 76 (2016), pp. 1000–1030.
- [2] M BARTELS, M KRENKEL, J HABER, RN WILKE, AND T SALDITT, *X-ray holographic imaging of hydrated biological cells in solution*, Phys. Rev. Lett., 114 (2015), p. 048103.
- [3] M BARTELS, M PRIEBE, RN WILKE, SP KRÜGER, K GIEWEKEMEYER, S KALBFLEISCH, C OLENDROWITZ, M SPRUNG, AND T SALDITT, *Low-dose three-dimensional hard X-ray imaging of bacterial cells*, Opt. Nanoscopy, 1 (2012), pp. 1–7.
- [4] HH BAUSCHKE, PL COMBETTES, AND DR LUKE, *Phase retrieval, error reduction algorithm, and Fienup variants: a view from convex optimization*, J. Opt. Soc. Am. A, 19 (2002), pp. 1334–1345.
- [5] A BURVALL, U LUNDSTRÖM, PAC TAKMAN, DH LARSSON, AND HM HERTZ, *Phase retrieval in X-ray phase-contrast imaging suitable for tomography*, Opt. Express, 19 (2011), pp. 10359–10376.
- [6] P CLOETENS, *Contribution to phase contrast imaging, reconstruction and tomography with hard synchrotron radiation: principles, implementation and applications*, PhD thesis, Vrije Universiteit Brussel, Brussels, Belgium, 1999.
- [7] P CLOETENS, W LUDWIG, J BARUCHEL, D VAN DYCK, J VAN LANDUYT, JP GUIGAY, AND M SCHLENKER, *Holotomography: Quantitative phase tomography with micrometer resolution using hard synchrotron radiation X-rays*, Appl. Phys. Lett., 75 (1999), pp. 2912–2914.
- [8] HP ERICKSON AND A KLUG, *Measurement and compensation of defocusing and aberrations by Fourier processing of electron micrographs*, Phil. Trans. R. Soc. B, 261 (1971), pp. 105–118.
- [9] JR FIENUP, *Phase retrieval algorithms: a personal tour*, Appl. Opt., 52 (2013), pp. 45–56.
- [10] D. GABOR ET AL., *A new microscopic principle*, Nature, 161 (1948), pp. 777–778.
- [11] K GIEWEKEMEYER, SP KRÜGER, S KALBFLEISCH, M BARTELS, C BETA, AND T SALDITT, *X-ray propagation microscopy of biological cells using waveguides as a quasipoint source*, Phys. Rev. A, 83 (2011), p. 023804.
- [12] JP GUIGAY, *Fourier-transform analysis of Fresnel diffraction patterns and in-line holograms*, Optik, 49 (1977), pp. 121–125.
- [13] TE GUREYEV, TJ DAVIS, A POGANY, SC MAYO, AND SW WILKINS, *Optical phase retrieval by use of first born- and rytov-type approximations*, Appl. Opt., 43 (2004), pp. 2418–2430.
- [14] V HAVIN AND B JÖRICKÉ, *The Uncertainty Principle in Harmonic Analysis*, Springer-Verlag, Berlin, 1994.
- [15] R HOFMANN, J MOOSMANN, AND T BAUMBACH, *Criticality in single-distance phase retrieval*, Opt. Express, 19 (2011), pp. 25881–25890.
- [16] P JAMING, *Nazarov’s uncertainty principles in higher dimension*, J. Approx. Theory, 149 (2007), pp. 30–41.
- [17] P JONAS AND AK LOUIS, *Phase contrast tomography using holographic measurements*, Inverse Probl., 20 (2004), p. 75.
- [18] MV KLIBANOV, *Phaseless inverse scattering problems in three dimensions*, SIAM J. Appl. Math., 74 (2014), pp. 392–410.
- [19] A KOSTENKO, J BATENBURG, A KING, SE OFFERMAN, AND LJ VAN VLIET, *Total variation minimization approach in in-line x-ray phase-contrast tomography*, Opt. Express, 21 (2013), pp. 12185–12196.
- [20] M KRENKEL, M TÖPPERWIEN, M BARTELS, P. LINGOR, D SCHILD, AND T SALDITT, *X-ray phase contrast tomography from whole organ down to single cells*, Proc. SPIE, (2014), p. 92120R.
- [21] M LANGER, P CLOETENS, A PACUREANU, AND F PEYRIN, *X-ray in-line phase tomography of multimaterial objects*, Opt. Lett., 37 (2012), pp. 2151–2153.
- [22] H LICHTÉ AND M LEHMANN, *Electron holography—basics and applications*, Rep. Prog. Phys., 71 (2007), p. 016102.
- [23] STEFANO MARCHESINI, *Invited article: A unified evaluation of iterative projection algorithms for phase retrieval*, Rev. Sci. Instrum., 78 (2007), p. 011301.
- [24] S MARETZKE, *Regularized Newton methods for simultaneous Radon inversion and phase retrieval in phase contrast tomography*, arXiv preprint, (2015), p. arXiv:1502.05073.
- [25] ———, *A uniqueness result for propagation-based phase contrast imaging from a single measurement*, Inverse Probl., 31 (2015), p. 065003.
- [26] S MARETZKE, M BARTELS, M KRENKEL, T SALDITT, AND T HOHAGE, *Regularized Newton methods for X-ray phase contrast and general imaging problems*, Opt. Express, 24 (2016), pp. 6490–6506.
- [27] SC MAYO, PR MILLER, SW WILKINS, TJ DAVIS, D GAO, TE GUREYEV, D PAGANIN, DJ PARRY,

- A POGANY, AND AW STEVENSON, *Quantitative X-ray projection microscopy: phase-contrast and multi-spectral imaging*, J. Microsc., 207 (2002), pp. 79–96.
- [28] J MIAO, T ISHIKAWA, IK ROBINSON, AND MM MURNANE, *Beyond crystallography: Diffractive imaging using coherent x-ray light sources*, Science, 348 (2015), pp. 530–535.
- [29] FL NAZAROV, *Local estimates for exponential polynomials and their applications to inequalities of the uncertainty principle type*, Algebra i Analiz, 5 (1993), pp. 3–66.
- [30] KA NUGENT, *X-ray noninterferometric phase imaging: a unified picture*, JOSA A, 24 (2007), pp. 536–547.
- [31] ———, *Coherent methods in the X-ray sciences*, Adv. Phys., 59 (2010), pp. 1–99.
- [32] D PAGANIN, *Coherent X-ray optics*, vol. 1, Oxford University Press, Oxford, 2006.
- [33] D PAGANIN, SC MAYO, TE GUREYEV, PR MILLER, AND SW WILKINS, *Simultaneous phase and amplitude extraction from a single defocused image of a homogeneous object*, J. Microsc., 206 (2002), pp. 33–40.
- [34] D PAGANIN AND KA NUGENT, *Noninterferometric phase imaging with partially coherent light*, Phys. Rev. Lett., 80 (1998), p. 2586.
- [35] A POGANY, D GAO, AND SW WILKINS, *Contrast and resolution in imaging with a microfocus X-ray source*, Rev. Sci. Instrum., 68 (1997), pp. 2774–2782.
- [36] HM QUINEY, *Coherent diffractive imaging using short wavelength light sources*, J. Mod. Opt., 57 (2010), pp. 1109–1149.
- [37] A RUHLANDT, M KRENKEL, M BARTELS, AND T SALDITT, *Three-dimensional phase retrieval in propagation-based phase-contrast imaging*, Phys. Rev. A, 89 (2014), p. 033847.
- [38] A RUHLANDT AND T SALDITT, *Three-dimensional propagation in near-field tomographic x-ray phase retrieval*, Acta Crystallogr. Sect. A, 72 (2016).
- [39] T SALDITT, M OSTERHOFF, M KRENKEL, RN WILKE, M PRIEBE, M BARTELS, S KALBFLEISCH, AND M SPRUNG, *Compound focusing mirror and x-ray waveguide optics for coherent imaging and nano-diffraction*, J. Synchrotron Radiat., 22 (2015), pp. 867–878.
- [40] D SLEPIAN, *Some comments on Fourier analysis, uncertainty and modeling*, SIAM Rev., 25 (1983), pp. 379–393.
- [41] D SLEPIAN AND E SONNENBLICK, *Eigenvalues associated with prolate spheroidal wave functions of zero order*, Bell Syst. Tech. J., 44 (1965), pp. 1745–1759.
- [42] L TURNER, B DHAL, J HAYES, A MANCUSO, K NUGENT, D PATERSON, R SCHOLTEN, C TRAN, AND A PEELE, *X-ray phase imaging: Demonstration of extended conditions for homogeneous objects*, Opt. Express, 12 (2004), pp. 2960–2965.
- [43] RH WADE, *A brief look at imaging and contrast transfer*, Ultramicroscopy, 46 (1992), pp. 145–156.
- [44] SW WILKINS, TE GUREYEV, D GAO, A POGANY, AND AW STEVENSON, *Phase-contrast imaging using polychromatic hard X-rays*, Nature, 384 (1996), pp. 335–338.